Establishing Predictive Indicators for Stability and Performance of SDOF Real-time Hybrid Simulations

Amin Maghareh, Shirley J. Dyke, Arun Prakash, and Jeffrey F. Rhoads

{amaghare, sdyke, aprakas, jfrhoads} @ purdue.edu

Report IISL – 004, December 2013

Abstract

Real-time hybrid simulation (RTHS) is increasingly being recognized as a powerful cyber-physical technique that offers the opportunity for system evaluation of civil structures subject to extreme dynamic loading. Advances in this field are enabling researchers to evaluate new structural components/systems in cost-effective and efficient ways, under more realistic conditions. In RTHS, the response of a structural system is simulated by partitioning it into physical and numerical substructures, and coupling at the interface is achieved by enforcing equilibrium and compatibility in real-time.

The choice of partitioning parameters will influence the overall success of the experiment. In addition, due to the dynamics of the transfer system, communication delays, and computation delays, the interaction force signals are dependent on the system state subject to delay. Thus, the transfer system dynamics must be accommodated by appropriate actuator controllers. In light of this, guidelines should be established to facilitate successful RTHS and clearly specify, (i) the minimum requirements of the transfer system control, (ii) the minimum required sampling frequency, and (iii) the most effective ways to stabilize an unstable simulation due to the limitations of the available transfer system. Moreover, to predict and evaluate the accuracy with various partitioning choices while incorporating the dynamics of the transfer system and computational/communication delays, performance indicators need to be developed.

In this study, new stability and performance indicators, predictive stability indicator (PSI) and predictive performance indicator (PPI), are proposed to predict the stability margin and performance of an RTHS system prior to its implementation. PSI and PPI assess how transfer system dynamics and computational/communication delays, which are the significant sources of systematic experimental error in RTHS, destabilize and distort RTHS responses. Moreover, along with the RTHS stability switch criterion, predictive stability and performance indicators might be used in developing acceptance criteria for conducting single-degree-of-freedom (SDOF) RTHS.

Acknowledgement: Financial support for this research was provided by the U.S. National Science Foundation under Grant NSF CCF-1136073.

Data presented herein will be available for download in the NEEShub(nees.org).

Contents

List of Figures

List of Tables

Chapter 1

Background

1.1 Introduction

As civil engineering structures evolve to meet the needs of future generations, there is an increasing demand to address ongoing challenges such as demonstrating the effectiveness of performance-based design, considering soil-structure interaction, utilizing new materials capable of reducing earthquake impact, and improving retrofitting strategies (Dyke et al., 2010). These challenges justify the need for extending and evolving our experimental capabilities for evaluating structural response and performance in a suitable and cost-effective manner. Currently, there exist three main experimental methods to evaluate structural behavior in the presence of dynamic loads, (1) shake table testing, (2) quasi-static testing, and (3) hybrid simulation (Mosqueda et al., 2005).

Shake table testing enables researchers to achieve realistic test conditions and evaluate critical issues such as collapse mechanisms, component failures, acceleration amplifications, residual displacements and post-earthquake capacities, independently (Schellenberg and Mahin, 2006). In the seismic evaluation of civil structures using shake table testing, a researcher needs to know the actuator's required peak velocity (directly related to the oil flow rate provided by the pumping system and servo-valve), the rated capacity of the actuator, the maximum stroke, and the actuator frequency bandwidth (Dihoru and Bonzi, 2010). To design a test considering these well-defined parameters, there is usually no stability concern, and the results are reliable. However, since very few shake tables in the world are capable of testing full-scale large civil structures and those experiments may be prohibitively expensive, shake table testing is usually limited to prototypes, limited in payload, and often conducted for critical parts of a structure at the component level (Shing et al., 1996).

Quasi-static testing is another experimental technique in which the structure (or the structural

component) under investigation is subject to a predefined displacement history at a slow rate. One of the most important advantages of the quasi-static testing compared to the shake table testing is that it does not require dynamic loading even though it is an experimental technique for evaluating the dynamic performance of structures. Since quasi-static loading actuators have much more capacity than dynamic actuators, the quasi-static technique enables researchers to conduct large- or full-scale experiments and closely observe the performance of the structure under investigation (Nakashima et al., 1992). Currently, this technique is usually applied to study the hysteretic and cyclic behavior of structural components subject to seismic loading (Carrion and Spencer, 2007). While quasi-static testing can be implemented on large civil structures, it has two major drawbacks, it requires a predefined displacement history (Shing and Mahin, 1984), and it does not preserve rate-dependence while evaluating the dynamic performance of structures.

Hybrid simulation (HS) is a cost-effective experimental technique used to evaluate the dynamic performance of large civil structures. In the late 80s, a number of researchers had shown that results of HS and shake table tests are comparable if experimental errors are effectively mitigated in conducting HS (Takanashi and Nakashima, 1987; Mahin et al., 1989). In hybrid simulation, the structure under investigation (i.e. the reference structure) is partitioned into two substructures, (i) a physical (or experimental) substructure, which usually includes the structure's more complex components, and (ii) a numerical (or analytical) substructure, which usually includes well-understood components. Coupling between the two substructures is achieved by enforcing equilibrium and compatibility at the interface (Chen et al., 2012). One of the critical assumptions for conducting HS is that the effect of loading rate on the interaction force of the numerical substructure is insignificant. This critical assumption has been validated for some structural materials, such as reinforced concrete and steel under certain conditions (Nakashima et al., 1992). However, with the introduction of new structural components and devices with rate-dependent behavior for seismic protection (e.g. rubber bearings, viscous dampers, friction dampers, sloshing dampers, magneto-rheological dampers, and electro-rheological dampers), conventional quasi-static testing and hybrid simulation are unable to effectively evaluate the dynamic performance of these rate-dependent structural components (Nakashima et al., 1992). Therefore, the need to examine the dynamic performance of rate-dependent structural components leads researchers to conduct fast hybrid simulation and real-time hybrid simulation.

Real-time hybrid simulation is a powerful experimental technique used to evaluate the performance of civil structures, especially, when rate-dependence plays a role. In RTHS, the interface interaction between the substructures is enforced by a transfer system which includes servo-hydraulic actuator(s) and/or a shake table (Wallace et al., 2005). The transfer system needs to be designed

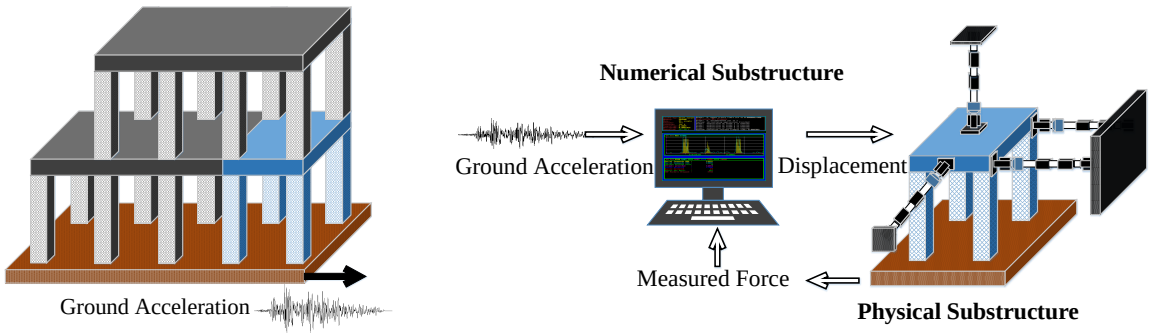

(a) Reference structure (b) Real-time hybrid simulation

Figure 1.1: A typical real-time hybrid simulation of a two-story structure.

and controlled such that all the interface boundary conditions are satisfied in real-time (Wagg and Stoten, 2001). Fig. 1.1 depicts a real-time hybrid simulation of a two-story structure where hydraulic actuators are used to achieve the interface boundary conditions.

A number of researchers have used this cyber-physical technique to successfully evaluate the seismic performance of structures, examine different structural control algorithms and techniques, and develop guidelines for the implementation of damping systems in civil infrastructures. Many examples of this can be found in the project repository of the George E. Brown Network for Earthquake Engineering Simulation (http://www.nees.org/). To name a few, Mosqueda, *et al.* evolved the use of more complex structural models employed in RTHS using geographically-distributed substructures and investigated the procedures for evaluating the reliability of the results in real-time (Mosqueda et al., 2007a,b, 2005). Christenson, *et al.* implemented RTHS to evaluate the relative efficacy of smart damping control devices (Christenson et al., 2008) and Shao, *et al.* conducted force-based substructuring in RTHS (Shao et al., 2011). Gao and Castaneda implemented and validated small-scale frame structural configurations equipped with damper devices to develop a robust framework for RTHS (Gao, 2012; Castaneda et al., 2012). In addition, Chae developed a performance-based design procedure for structures with MR dampers using RTHS (Chae, 2011).

RTHS is a complex cyber-physical technique, and the configuration of the test affects how well the researcher is able to achieve his/her goals. Stability and performance of RTHS are mainly a function of four conditions, (1) the overall dynamics of the reference structure, (2) the fidelity of the numerical substructure, (3) how the reference structure is partitioned into the numerical and physical substructures, and (4) how well the interface boundary conditions are enforced by the transfer system. Several researchers have investigated the impact of these entities on stability and accuracy of simulations (Darby et al., 2002; Mosqueda et al., 2007a,b; Chen and Ricles, 2009a;

Gao, 2012; Chen et al., 2013; Maghareh et al., 2012). Furthermore, to complete the work carried out on stability of RTHS systems, Maghareh, *et al.* proposed a pre-experiment performance metric, predictive performance indicator (PPI), to predict the performance of RTHS systems prior to its implementation (Maghareh et al., 2013).

Errors occur in RTHS from three different sources, model idealization, numerical integration, and experimental errors. First, modeling error arises from any discrepancies between the response of the actual (or real) portion modeled as numerical substructure and the response acquired from its model. Second, in RTHS, explicit or implicit integration schemes are utilized to solve the idealized numerical substructure. A very significant characteristic of the explicit methods, which makes it more attractive for conducting RTHS, is that with this approach all the numerical computations are processed in a consistent predictable amount of time. Using explicit schemes, the next state of the structure is computed merely based on the current state and the input. In HS and RTHS, the fact that in the explicit schemes the actuator command is computed without prior knowledge of the system's response is a major source of numerical error. Depending upon which integration scheme is adopted, stability and accuracy issues may be limiting factors (Mosqueda et al., 2005). Moreover, in the implementation of RTHS with more sophisticated reference structures (particularly, the numerical substructure), parallel scheduling has become increasingly important due to the advances in multiprocessor systems and the high computational demand in the numerical substructure. In an attempt to address this issue, Li, *et al.* designed, implemented and evaluated a practical real-time platform that efficiently runs sporadic parallel task sets with implicit deadlines (Li et al., 2013). Finally, in RTHS, there are a number of experimental sources of error which can be categorized as epistemic (or systematic) and aleatoric (or random) errors. Sources of epistemic errors are systematic, such as transfer system dynamics, computational delays, communication delays, and sensor miscalibration. However, sources of aleatoric errors are random, such as measurement noise and random truncations in the analog-to-digital (AD) conversions of signals.

Existing RTHS performance (or accuracy) indicators can be divided into three categories, (i) indicators computed prior to an experiment (pre-experiment) to enable a researcher to predict the susceptibility of an RTHS configuration to any systematic or random sources of error, (ii) indicators computed during the experiment (online) to enable a researcher to evaluate the quality of RTHS responses and detect unacceptable results in real-time, and (iii) indicators computed after the experiment (post-experiment) to enable a researcher to assess the quality of RTHS responses with respect to reference responses in the RTHS data analysis process. Pre-experiment indicators are necessary for users to assess the accuracy of RTHS responses, to develop the minimum requirements with respect to any user-defined acceptance criterion, and to assist researchers in enhancing

the performance of RTHS responses more effectively. Thus, a number of researchers developed techniques to determine and alleviate the impact of the systematic errors in RTHS on the overall performance of the system. To name a couple, Horiuchi, *et al.* have developed an effective viscous damping for a linear elastic specimen and a constant feedback delay (Horiuchi et al., 1999) and Mosqueda, *et al.* estimated the effective damping ratio of a SDOF RTHS with a constant time delay (Mosqueda et al., 2007b). Later, an online energy indicator, hybrid simulation error monitors (HSEM), was developed to assess the quality of RTHS responses in real-time (Mosqueda et al., 2007a,b). In these studies, Mosqueda, *et al.* investigated the impact of experimental errors on linear and nonlinear seismic responses of structures using HSEM. Moreover, this indicator also serves as a basis for an RTHS safety system to cease the simulation, examine the source of error, and possibly correct the issue. Finally, towards RTHS data analysis process and in the presence of reference responses, researchers have been using a number of time-based or frequency-based indicators to assess the quality of RTHS responses.

In this report, chapter one and two are focused on modeling and stability of SDOF RTHS system, respectively. In chapter one, RTHS is modeled by a set of delay differential equations (DDEs). The objective of chapter two is twofold, (i) to establish an RTHS stability switch criterion, and (ii) to develop an RTHS design guideline associated with the minimum requirements for the transfer system control and sampling frequency. The main parameters investigated in this chapter are, (1) the structural characteristics of the reference structure (e.g. natural frequency, damping ratio, and structural nonlinearity), (2) the partitioning parameters, and (3) the transfer system time delay associated with the feedback force signal. Finally, in this chapter, we propose a new stability indicator, predictive stability indicator (PSI), to predict the stability margin of a SDOF RTHS configuration. In chapter three, the objective is to propose a new performance indicator, predictive performance indicator (PPI), to predict the performance of an RTHS system prior to its implementation. This metric assesses how transfer system dynamics and computational/communication delays, which are the significant sources of systematic experimental error in RTHS, distort RTHS responses and how the corresponding error propagates through the entire RTHS. This indicator is developed in a way to be reconcilable with the RTHS stability switch criterion. Moreover, along with the RTHS stability switch criterion, the PSI and PPI may be utilized to establish a pre-experiment acceptance criteria in RTHS. In chapter four, the utility of the RTHS stability switch criterion, PSI, and PPI is illustrated by providing three different types of examples, virtual RTHS with pure time delay, virtual RTHS with time delay and transfer system dynamics, and an actual RTHS example. Finally, chapter five contains concluding remarks on the proposed predictive indicators for stability and performance of SDOF RTHS.

1.2 Modeling of RTHS Systems

The governing equation of a general reference structure can be expressed as

$$[M]\ddot{X}(t) + [C]\dot{X}(t) + R(X) = -[M]\Gamma\ddot{x}_g(t) \tag{1.1}$$

where $[M]$, $[C]$, $R(X)$, Γ, $X(t)$, and $\ddot{x}_g(t)$ are the structure's mass matrix, damping matrix, restoring force vector, influence vector, displacement vector, and ground acceleration, respectively. In RTHS, the reference structure is partitioned into numerical and physical substructures

$$\{[M],[C],R(X)\} = \{[M_p],[C_p],R_p(X)\} + \{[M_n],[C_n],R_n(X)\} \tag{1.2}$$

where p and n indices refer to the physical and numerical substructures. The governing equation of the numerical substructure can be expressed as

$$[M_n]\ddot{X}(t) + [C_n]\dot{X}(t) + R_n(X) = -[M]\Gamma\ddot{x}_g(t) - F_{fb}(t) \tag{1.3}$$

where $F_{fb}(t)$ is the interaction force (or feedback force) vector measured in the physical substructure and used as a feedback signal into the numerical substructure. In an ideal case, $F_{fb}(t)$ can be defined as

$$F_{fb}(t) = [M_p]\ddot{X}(t) + [C_p]\dot{X}(t) + R_p(X). \tag{1.4}$$

Combining Eqs. (1.3) and (1.4) yields the governing equation of the reference structure in Eq. (1.1). However, the ideal case requires perfect control of the transfer system, no measurement noise, no time delay, and that all the boundary conditions are satisfied perfectly. Due to transfer system control limitations and computational/communication time delay, the governing equation of an RTHS system becomes

$$[M_n]\ddot{X}(t) + [C_n]\dot{X}(t) + R_n(X) = -[M]\Gamma\ddot{x}_g(t) - T\{\sum a_i F_{fb}(t-\tau_i), \sum b_i \dot{F}_{fb}(t-\tau_i), \ldots\} \tag{1.5}$$

where $T\{\ldots\}$ is an operator representing the effect of the transfer system dynamics and $F_{fb}(t-\tau)$ indicates time delay in the interaction force signal.

In RTHS, time lags and time delays can be classified into three major categories, (1) communication delays, (2) computational delays, and (3) transfer system dynamics. No matter which control (or compensation) strategy is adopted, there is always a frequency-dependent phase shift between the command input and the realization of the command by the transfer system which is

referred as time lag (or system dynamics). Time delay and system dynamics are two different concepts which are sometimes used interchangeably. Fig. 1.2 demonstrates a general distributed RTHS architecture with multiple physical and numerical substructures. In addition, the presence of the communication and computational delays and transfer system dynamics are shown.

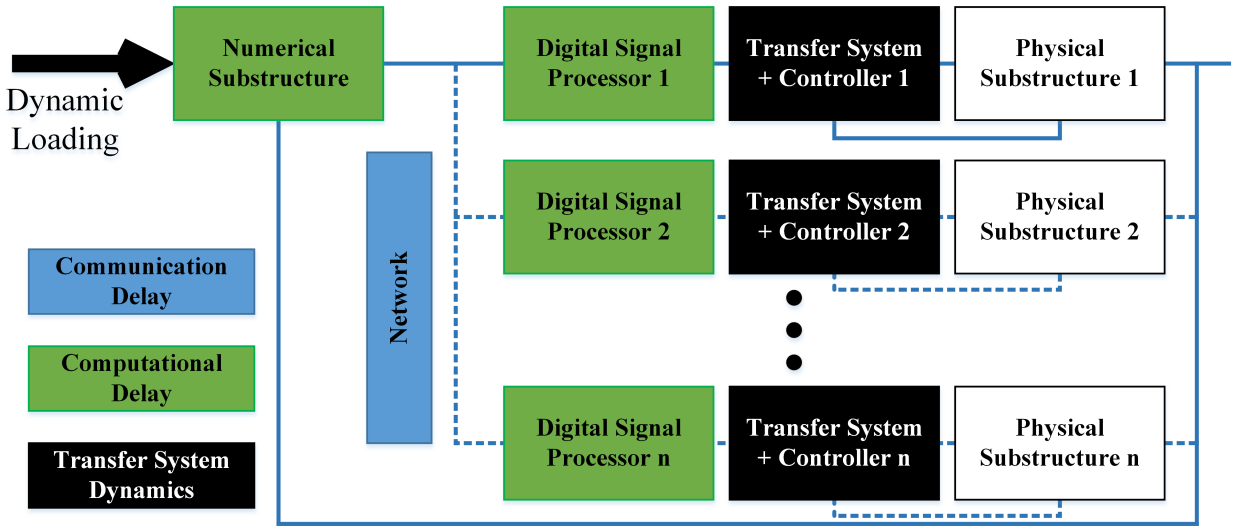

Figure 1.2: General distributed RTHS architecture.

1.2.1 Communication Delay

To implement RTHS, there is a continuous exchange of information between the cyber and physical components. In RTHS, communication delays vary from almost negligible for an RTHS using a single processor (no network) to more than a hundred milliseconds for geographically-distributed testing. Geographically-distributed RTHS presents a challenge in which the required communication over the internet results in random delays (Mosqueda et al., 2005). Thus, communication delays become especially significant when conducting geographically-distributed RTHS (Carrion and Spencer, 2007), see Fig. 1.3.

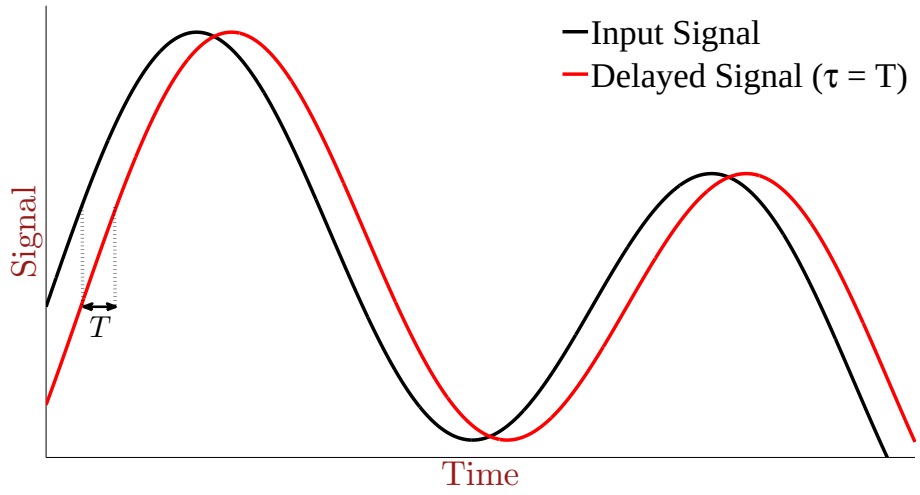

Figure 1.3: Communication delay.

1.2.2 Computational Delay

In RTHS, integration schemes are implemented to solve the discretized governing equation of the numerical substructure. Stability and performance issues are limiting factors which determine the maximum permissible computational time and the largest natural frequency of the numerical model in a linear case. In RTHS, all computations are executed on processors and then the command signal is implemented using a digital-to-analog convertor (DAC). One of the most common methods is the zero-order hold method (ZOH) shown in Fig. 1.4. In this method, the signal is held constant during the integration time-step. The transfer function of the ZOH method can be expressed as

$$H_{ZOH}(s) = \frac{1 - e^{-sT}}{sT} \tag{1.6}$$

where $s \in \mathbb{C}$ is the Laplace variable and T is the integration time-step. By applying the Tylor expansion, $H_{ZOH}(s)$ can be written as

$$H_{ZOH}(s) = \frac{1 - (1 - sT + (sT)^2/2 + o(T^3))}{sT} = 1 - \frac{sT}{2} + o(T^2). \tag{1.7}$$

For a relatively small integration time-step, Eq. (1.7) can be approximated with

$$H_{ZOH}(s) = 1 - \frac{sT}{2} + o(T^2) \approx e^{-sT/2}. \tag{1.8}$$

Thus, the effect of the ZOH conversion on the signal is approximately equal to that of a time delay of $T/2 = (2f_s)^{-1}$ where f_s is the sampling frequency in Hz.

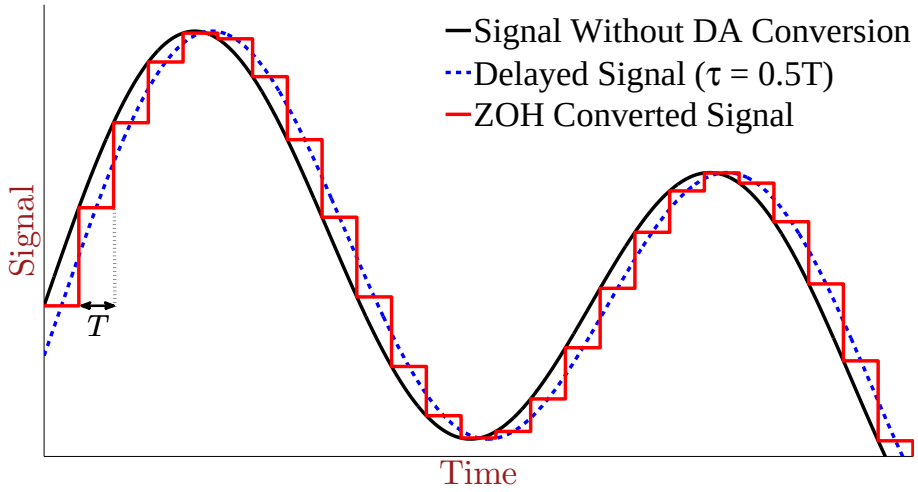

Figure 1.4: Computational delay.

1.2.3 Transfer System Dynamics

No matter which control strategy is adopted, there is always a time lag between the command input and the realization of the command by the transfer system which is usually frequency dependent. Furthermore, Dyke, *et al.* analyzed the effects of control-structure interaction (CSI) and demonstrated that the dynamics of a hydraulic actuator, a common type of transfer system in RTHS, and the plant are coupled through a natural velocity feedback, see Fig. 1.5. So, the time lag is caused by both actuator dynamics and the attached specimen (Dyke et al., 1995) and is not a pure time delay. However, the contribution of the actuator dynamics is dominant (Zhao et al., 2003) and within a typical seismic frequency bandwidth, experimental studies have demonstrated that a linearized actuator model can capture the essential dynamics of the actuator (Gao, 2012).

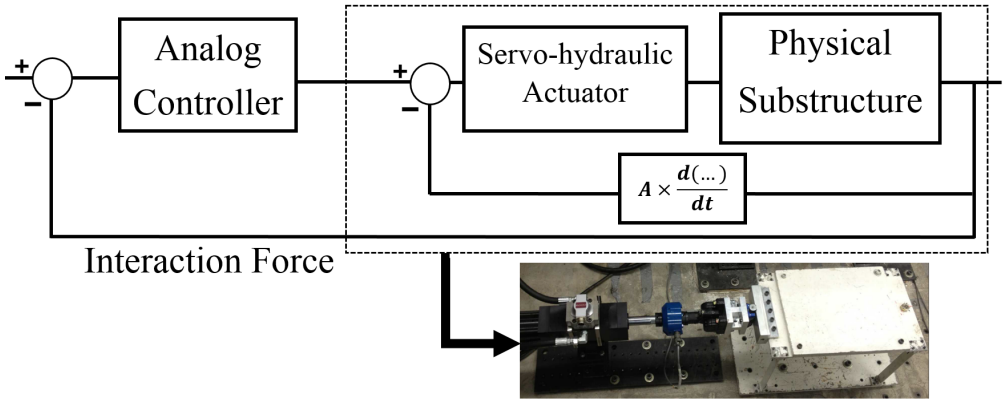

Figure 1.5: Control-structure Interaction.

Typically, for a SDOF RTHS, the natural frequency of the attached specimen in RTHS is large compared to the seismic frequency bandwidth. Therefore, the phase of the actuator frequency response function can be approximated as linear and modeled as a pure time delay (Carrion and Spencer, 2007). Typical values for actuator time lags reported in the literature range from 8 to 30 msec (Horiuchi et al., 1999; Darby et al., 2002; Shing et al., 2004).

Figure 1.6: Servo-hydraulic actuator as a common transfer system.

1.2.4 Time Delay and System Dynamics (or Time Lag)

Time delay and system dynamics are two different concepts which are sometimes used interchangeably. To delineate the difference, this work compares the dynamics of a servo-hydraulic actuator model with a time delay system in the frequency domain. A time delay system, and a linear system dynamics can be mathematically expressed as

$$x(t) = u(t - \tau) \tag{1.9a}$$

$$x^{(n)}(t) + \ldots + a_0 x(t) = b_m u^{(m)}(t) + \ldots + b_1 u(t) + b_0 \tag{1.9b}$$

where $u(t)$, $x(t)$ and τ are the system input, system output and time delay value, respectively. A very common type of transfer system in RTHS is a controlled servo-hydraulic actuator. For a more realistic comparison, a servo-hydraulic actuator shown in Fig. 1.6, was identified at the Intelligent Infrastructure System Lab (*IISL*) at Purdue University. The identified dynamics of the servo-hydraulic actuator, which corresponds to measured displacement to command displacement, is given by

$$\frac{x_{msd}(s)}{x_{cmd}(s)} = \frac{2.382 \times 10^9}{s^4 + 485.5s^3 + 1.317 \times 10^5 s^2 + 3.182 \times 10^7 s + 2.382 \times 10^9} \tag{1.10}$$

Fig. 1.7 provides the frequency responses of the servo-hydraulic actuator and a pure time delay system.

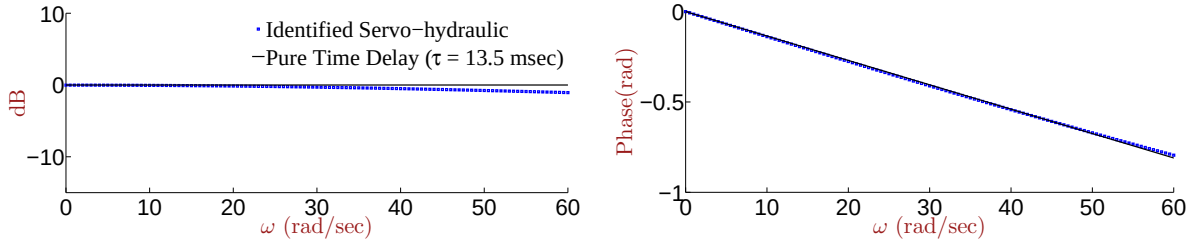

(a) Magnitude plot (b) Phase plot

Figure 1.7: Frequency responses of the hydraulic actuator and a pure time delay system.

Clearly, over a relatively low frequency bandwidth, the responses of the pure time delay and transfer system dynamics are quite similar. In RTHS, the frequency bandwidth of interest is the seismic frequency bandwidth and it is restricted to a low frequency bandwidth. Therefore, over a relatively low frequency bandwidth, we can model the dynamic interaction of a transfer system and the physical substructure with a constant time delay (Christenson et al., 2008; Maghareh et al., 2012). Thus, in this study on SDOF systems, Eq. (1.5) is replaced by Eqs. (1.11a) and (1.11b) in which the communication delay, computational delay, and transfer system dynamics are all lumped into a single time delay (τ) which acts upon the interaction force signal.

$$[M_n]\ddot{x}(t) + [C_n]\dot{x}(t) + R_n(x) = -[M]\Gamma\ddot{x}_g(t) - F_{fb}(t-\tau) \tag{1.11a}$$

$$F_{fb}(t) = [M_p]\ddot{x}(t) + [C_p]\dot{x}(t) + R_p(x) \tag{1.11b}$$

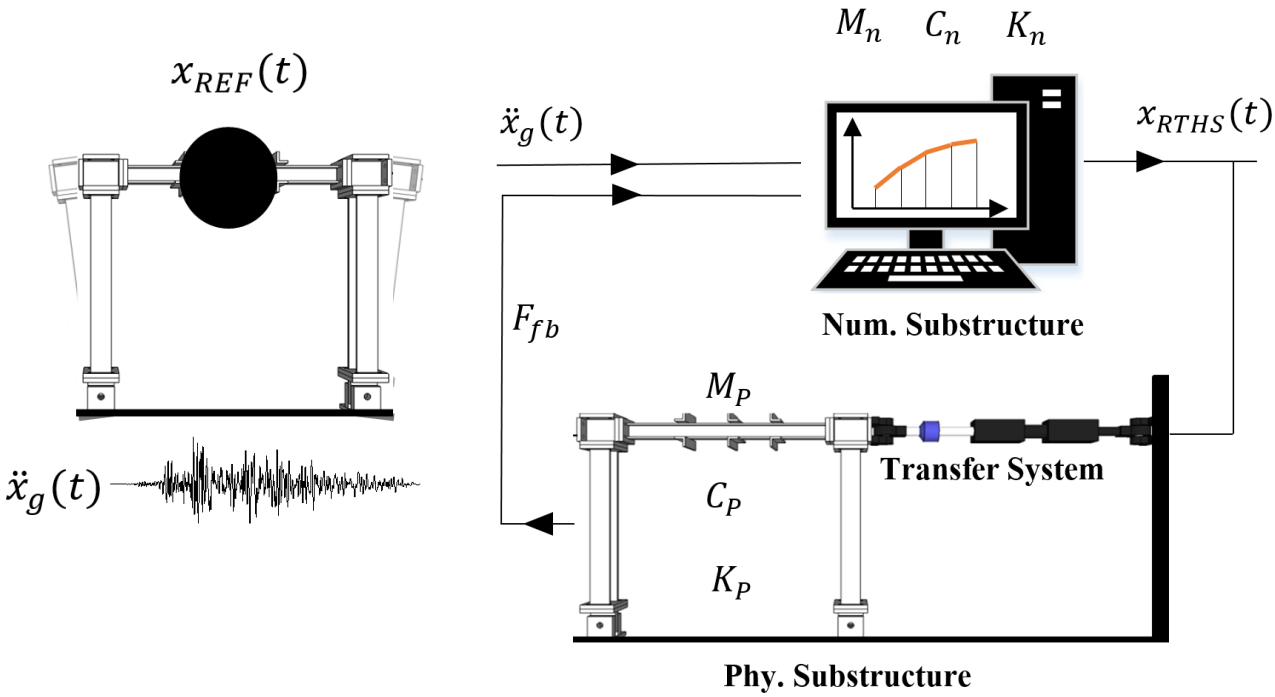

(a) Reference Structure (b) Real-time Hybrid Simulation

Figure 1.8: Schematic diagram of a SDOF RTHS.

1.3 Single-Degree-of-Freedom RTHS

Consider a linear single-degree-of-freedom (SDOF) reference structure with a seismic excitation input, as follows

$$M\ddot{x}(t) + C\dot{x}(t) + Kx = -M\ddot{x}_g(t) \tag{1.12}$$

where M, C,and K are the reference structure's mass, damping, stiffness, respectively.

For a SDOF RTHS, the reference structure is partitioned into the numerical and physical substructures, as shown in Fig. 1.8. The governing equation of the SDOF RTHS shown in Fig. 1.8, is approximated as a delay differential equation of the form

$$M_n\ddot{x}(t) + C_n\dot{x}(t) + K_n x = -M\ddot{x}_g(t) - F_{fb}(t-\tau) \tag{1.13a}$$

$$F_{fb}(t) = M_p\ddot{x}(t) + C_p\dot{x}(t) + K_p x. \tag{1.13b}$$

Eqs. (1.13a) and (1.13b) provide a basis for (i) investigating the impact of time delay on the modal characteristics of a SDOF RTHS, and (ii) establishing stability and performance metrics for

effective RTHS implementation.

Chapter 2

Stability

To conduct a stability analysis of linear RTHS systems, a general geometric stability switch criterion in delay differential equations can be implemented to establish an RTHS stability switch criterion. A more detailed discussion on the general geometric stability switch criterion is provided in (Wallace et al., 2005; Beretta and Kuang, 2002).

2.1 An RTHS Stability Switch Criterion

Consider a linear single-degree-of-freedom (SDOF) reference structure with a seismic excitation, as follows.

$$M\ddot{x}(t) + C\dot{x}(t) + Kx = -M\ddot{x}_g(t) \tag{2.1}$$

where M, C,and K are the reference structure's mass, damping, and stiffness, respectively. For SDOF RTHS, the reference structure is partitioned into numerical and physical substructures, as shown in Fig. 1.8. The governing equation of the SDOF RTHS shown in Fig. 1.8 is

$$M_n\ddot{x}(t) + C_n\dot{x}(t) + K_n x = -M\ddot{x}_g(t) - F_{fb}(t-\tau) \tag{2.2a}$$

$$F_{fb}(t) = M_p\ddot{x}(t) + C_p\dot{x}(t) + K_p x. \tag{2.2b}$$

To study the response of this RTHS system, we use the Laplace transform in which

$$\mathcal{L}[\ldots](s) = \int_{-\infty}^{\infty} \ldots e^{-st}\mathrm{d}t \tag{2.3}$$

where $s \in \mathbb{C}$ is the Laplace variable. The response of the reference structure, Eq. (2.1), is given by

$$x_{REF}(s) = \frac{-M}{Ms^2 + Cs + K}\ddot{x}_g(s) \tag{2.4}$$

In the absence of a feedback time delay ($\tau = 0$), the response of the RTHS system in Fig. 1.8 can be expressed as

$$x_{RTHS}(s) = \frac{-M}{M_n s^2 + C_n s + K_n}\ddot{x}_g(s) - \frac{M_p s^2 + C_p s + K_p}{M_n s^2 + C_n s + K_n}x_{RTHS}(s) \tag{2.5}$$

therefore,

$$\frac{Ms^2 + Cs + K}{M_n s^2 + C_n s + K_n}x_{RTHS}(s) = \frac{-M}{M_n s^2 + C_n s + K_n}\ddot{x}_g(s) \tag{2.6}$$

and

$$x_{RTHS}(s) = x_{REF}(s) = \frac{-M}{Ms^2 + Cs + K}\ddot{x}_g(s) \tag{2.7}$$

Thus, in the absence of feedback time delay, the response of an RTHS system is identical to the response of the reference structure. However, in the presence of feedback time delay, the response of the RTHS system is

$$x_{RTHS}(s) = \frac{-M}{(M_n s^2 + C_n s + K_n) + (M_p s^2 + C_p s + K_p)e^{-\tau s}}\ddot{x}_g(s) \tag{2.8}$$

and the resulting characteristic equation can be written as

$$\Gamma(\lambda, \tau) = (M_n\lambda^2 + C_n\lambda + K_n) + (M_p\lambda^2 + C_p\lambda + K_p)e^{-\tau\lambda} \tag{2.9}$$

where $\lambda \in \mathbb{C}$. Eq. (2.9) can be expressed as

$$\Gamma(\lambda, \tau) = \Gamma_n(\lambda) + \Gamma_p(\lambda)e^{-\tau\lambda}. \tag{2.10}$$

For a dynamic system to be asymptotically stable about its fixed points, all eigenvalues, which are the roots of the corresponding characteristic equation, must lie in the left half of the complex plane. Therefore, stability switching occurs when a root of the characteristic equation crosses the imaginary axis (i.e. $Re(\lambda_i) = 0$) as some parameters vary in the characteristic equation. If the partitioning parameters of the RTHS are chosen such that any root of the characteristic equation is in the right half of the complex plane, then that test configuration will be unstable.

Without loss of generality, it is assumed that the reference structure ($\tau = 0$) is stable (i.e. the roots of $\Gamma(\lambda, 0)$ in Eq. (2.10) lie in the left half of the complex plane). Next, we introduce two

new terms which are crucial in the theory of delay differential equations, (1) critical frequency ($\omega_{cr} = |\lambda_{cr}|$) which is the frequency at which a stability switch occurs, and (2) critical time delay (τ_{cr}) which is the time delay associated with the occurrence of a stability switch. In Eq. (2.10), to obtain the critical frequency and critical time delay associated with Eq. (2.10), one can simply replace λ, τ with $j\omega_{cr}$, τ_{cr} and equate $\Gamma(j\omega_{cr}, \tau_{cr})$ with 0, and express the characteristic equation as

$$-\frac{\Gamma_n(j\omega_{cr})}{\Gamma_p(j\omega_{cr})} = e^{-j\tau_{cr}\omega_{cr}} = e^{-j\Omega_{cr}} \tag{2.11}$$

where j is the imaginary unit number and Ω_{cr} is the product of the critical frequency and its corresponding critical time delay ($\Omega_{cr} = \tau_{cr}\omega_{cr}$). Eq. (2.11) can be solved using the geometric construction presented in (MacDonald, 1989). As Ω_{cr} increases from 0 to 2π, $e^{-j\Omega_{cr}}$ traces out a unit circle in the complex plane and the left hand side of the equation, which is called *the ratio curve*, traces out another curve. A stability switch occurs in the system when the unit circle intersects the ratio curve. The intersection can occur multiple times, meaning that the system is stable within a particular range of time delay, then it will be unstable for a specific range of time delay, and then the system may gain its stability back as the time delay increases, see Fig. 2.1. For RTHS, the first occurrence of the instability condition is the most meaningful. Using Eqs. (2.9), (2.10), and (2.11) the characteristic equation of a SDOF RTHS can be expressed as

$$\frac{-M_n{\omega_{cr}}^2 + C_n\omega_{cr}j + K_n}{-M_p{\omega_{cr}}^2 + C_p\omega_{cr}j + K_p} = e^{-j\tau_{cr}\omega_{cr}} \tag{2.12}$$

Using Euler's formula (i.e. $e^{\cdots j} = \cos\ldots + j\sin\ldots$), Eq. (2.12) can be written as

$$(-M_n{\omega_{cr}}^2 + C_n\omega_{cr}j + K_n) + (-M_p{\omega_{cr}}^2 + C_p\omega_{cr}j + K_p)(\cos(\tau_{cr}\omega_{cr}) - j\sin(\tau_{cr}\omega_{cr})) = 0 \tag{2.13}$$

Separating the real and imaginary parts of Eq. (2.13) yields the following system of equations

$$(K_p - M_p{\omega_{cr}}^2)\cos(\tau_{cr}\omega_{cr}) + C_p\omega_{cr}\sin(\tau_{cr}\omega_{cr}) = M_n{\omega_{cr}}^2 - K_n \tag{2.14a}$$

$$C_p\omega_{cr}\cos(\tau_{cr}\omega_{cr}) - (K_p - M_p{\omega_{cr}}^2)\sin(\tau_{cr}\omega_{cr}) = -C_n\omega_{cr}. \tag{2.14b}$$

Dividing both sides of Eqs. (2.14a) and (2.14b) by M yields

$$\{(1-\gamma)\omega_n^2 - (1-\alpha)\omega_{cr}^2\}\cos(\tau_{cr}\omega_{cr}) + \{2(1-\beta)\omega_{cr}\zeta\omega_n)\}\sin(\tau_{cr}\omega_{cr}) = \alpha\omega_{cr}^2 - \gamma\omega_n^2 \tag{2.15a}$$

$$\{2(1-\beta)\omega_{cr}\zeta\omega_n)\}\cos(\tau_{cr}\omega_{cr}) - \{(1-\gamma)\omega_n^2 - (1-\alpha)\omega_{cr}^2)\}\sin(\tau_{cr}\omega_{cr}) = -2\omega_n\zeta\omega_{cr}\beta \tag{2.15b}$$

where $\{\alpha, \beta, \gamma\} = \{M_n/M, C_n/C, K_n/K\}$ are the partitioning parameters and ζ is damping ratio. Eqs. (2.15a) and (2.15b) are squared and added together to obtain a 4^{th} order equation governing how the partitioning factors and the structural characteristics of the reference structure determine the critical frequency of the RTHS system (ω_{cr}),

$$(1-2\alpha){\omega_{cr}}^4 + {\omega_n}^2[4(1-2\beta)\zeta^2 - 2(1-\alpha-\gamma)]{\omega_{cr}}^2 + (1-2\gamma){\omega_n}^4 = 0. \tag{2.16}$$

Furthermore, Eq. (2.16) is normalized with respect to ω_n yielding

$$(1-2\alpha){\phi_{cr}}^4 + [4(1-2\beta)\zeta^2 - 2(1-\alpha-\gamma)]{\phi_{cr}}^2 + (1-2\gamma) = 0 \tag{2.17}$$

where $\phi_{cr} = \omega_{cr}/\omega_n$ is the critical frequency ratio. Eq. (2.17) may lead to 0, 1, or 2 meaningful critical frequencies (i.e. positive real values). The lowest of the three is associated with the limit of an unconditionally stable RTHS system. After obtaining ϕ_{cr} from Eq. (2.17), one can solve for the corresponding critical time delays using Eqs. (2.15a) and (2.15b).

$$\tau_{cr} = {\omega_{cr}}^{-1}[N\pi + \tan^{-1}(\frac{A}{B})] \tag{2.18a}$$

in which

$$A = [2(1-\beta)\omega_{cr}\zeta\omega_n)][\alpha{\omega_{cr}}^2 - \gamma{\omega_n}^2] + [(1-\gamma){\omega_n}^2 - (1-\alpha{\omega_{cr}}^2]2\omega_n\zeta\omega_{cr}\beta \tag{2.18b}$$

$$B = [(1-\gamma){\omega_n}^2 - (1-\alpha){\omega_{cr}}^2][\alpha{\omega_{cr}}^2 - \gamma{\omega_n}^2] - [2(1-\beta)\omega_{cr}\zeta\omega_n)]2\omega_n\zeta\omega_{cr}\beta \tag{2.18c}$$

where $N = 0, 1, 2, \ldots$ and making sure that Eqs. (2.15a) and (2.15b) are both achieved. Furthermore, Eq. (2.18a) is normalized with respect to ω_n and it becomes

$$\Omega_{cr} = \tau_{cr}\omega_n = {\phi_{cr}}^{-1}[N\pi + \tan^{-1}(\frac{A}{B})] \tag{2.19a}$$

$$A{\omega_n}^{-4} = [2(1-\beta)\phi_{cr}\zeta)][\alpha{\phi_{cr}}^2 - \gamma] + [(1-\gamma) - (1-\alpha){\phi_{cr}}^2]2\zeta\phi_{cr}\beta \tag{2.19b}$$

$$B{\omega_n}^{-4} = [(1-\gamma) - (1-\alpha){\phi_{cr}}^2[\alpha{\phi_{cr}}^2 - \gamma] - [2(1-\beta)\phi_{cr}\zeta)]2\phi_{cr}\zeta\beta. \tag{2.19c}$$

Thus, Eqs. (2.17) and (2.19a) can be used to find the stability characteristics of an RTHS system as a function of the partitioning parameters and the structural characteristics of the reference structure. However, it is recommended to first plot the RTHS stability diagram using Eqs. (2.17) and (2.19a), and then determine the stability characteristics of the RTHS system.

2.1.1 Stability Diagrams for a Linear SDOF RTHS

This section examines how the values of the partitioning parameters and the structural characteristics of the reference structure affect the stability of a linear RTHS system through the use of RTHS stability diagrams. Four sample partitioning cases will be considered, see Table 2.1. In Fig. 2.1, the stability diagrams associated with these sample cases, for 5 different reference damping ratios (a total of $4 \times 5 = 20$ systems) are examined.

Table 2.1: Partitioning parameters of the nine cases examined

	α factor	β factor	γ factor
Case I	$\in [0, 1]$	0.4	0.9
Case II	0.9	0.6	$\in [0, 1]$
Case III	$\in [0, 1]$	0.6	0.1
Case IV	0.1	0.4	$\in [0, 1]$

Practically speaking, a more realistic partitioning configuration is one where a majority of the mass is modeled in the numerical substructure (i.e. $\alpha \approx 1$) and a majority of the stiffness is placed in the physical substructure (i.e. $\gamma \approx 0$). Therefore, the bottom portion of Fig. 2.1b and the top portion of Fig. 2.1c represent more realistic scenarios. As shown in Fig. 2.1, the more realistic cases, where $\alpha \approx 1$ and $\gamma \approx 0$, are quite challenging configurations in terms of leading to small values of Ω_{cr}. Some important observations can be made from Fig. 2.1.

- For a specific ζ, the area to the left of the first curve is considered a stable region in RTHS (i.e. $\Omega < \Omega_{cr}$).
- The critical time delay is inversely proportional to the natural frequency of the reference structure. Thus, higher modes of the reference structure are highly sensitive to time delays. Often for multi-degree-of-freedom systems, higher modes are suppressed with artificial damping in the numerical substructure (Shing and Mahin, 1984).
- In selecting the partitioning parameters, $\alpha \approx 0.5$ is not a good choice from stability and performance perspectives, see Figs. 2.1a and 2.1c.
- For a particular RTHS configuration, multiple Ω_{cr} exist. Clearly, a stability switch occurs in the system when the unit circle in Eq. (2.11) intersects the ratio curve, and this can occur multiple times. Thus, the system is stable within a particular range of Ω, then it will be unstable for a specific range of Ω, and then the system will again be stable as Ω increases.

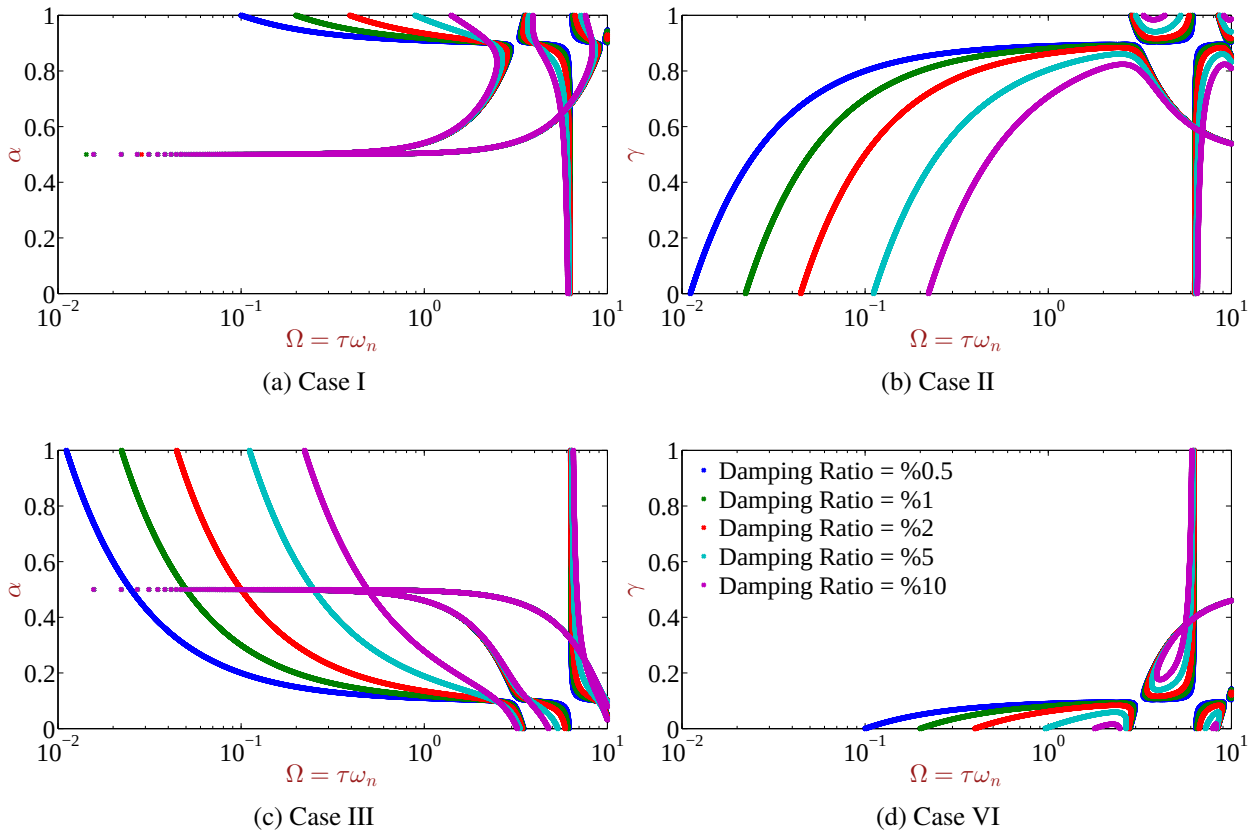

(a) Case I (b) Case II

(c) Case III (d) Case VI

Figure 2.1: Normalized RTHS stability diagrams showing Ω_{cr}.

Although the system may be stable at higher Ω, performance is likely to suffer. Therefore, it is recommended that to conduct an effective RTHS, users should consider just the first region of stability.

- As a rule of thumb, the value of critical time delay is closely related to $|\gamma - \alpha|$. Thus, larger value of $|\gamma - \alpha|$ usually leads to a relatively small critical time delay value.
- Critical time delay usually increases as the reference structure becomes more damped.
- Finally, if stability concerns lead to some changes in a partitioning setup, reducing $|\gamma - \alpha|$ and ω_n and/or increasing ζ are effective options.

2.1.2 Predictive Stability Indicator (PSI)

Herein, we build on the RTHS stability switch criterion and propose a stability metric which indicates the global stability margin of a SDOF RTHS system with any partitioning choice. For a

system with the characteristic equation of the form Eq. (2.10), a stability switch occurs when the unit circle intersects the ratio curve and the intersection can occur multiple times. However, to develop a stability indicator, the first occurrence of the instability is the most meaningful one. For a SDOF system of the form Eqs. (2.2a) and (2.2b), the predictive stability indicator can be written as

$$PSI = \log_{10}(\frac{10^3 \times min[\Omega_{cr}]}{\omega_n}) = \log_{10}(min[\tau_{cr}(msec)]). \tag{2.20}$$

It should be noted that Eq. (2.20) returns a meaningful value only for the first region of stability in the RTHS stability diagrams which is the region of interest herein. Therefore, in Eq. (2.21), we use $\min\{\Omega_{cr}\}$ to refer to the switching value of the first region of stability. As shown in Fig. 2.2, PSI spans between $-\infty$ and $+\infty$ corresponding to the case on the verge of instability to the unconditionally stable case.

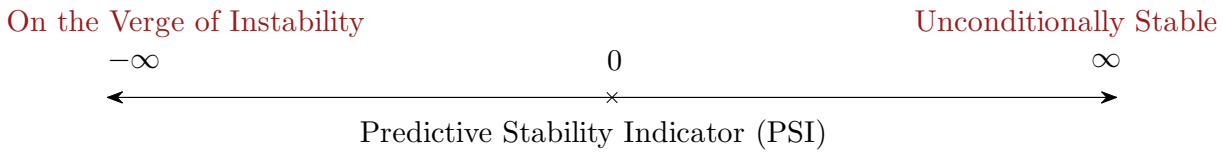

Figure 2.2: Predictive stability indicator (PSI) span.

To illustrate how the PSI values are obtained from the RTHS stability diagrams, Figs. 2.3a and 2.3b illustrate the stability diagrams corresponding to configuration 1: $\{\alpha = 0.7, \beta = 0.4, \gamma = 0.9, \zeta = 0.1\}$ and configuration 2:$\{\alpha = 0.9, \beta = 0.6, \gamma = 0.7, \zeta = 0.05\}$.

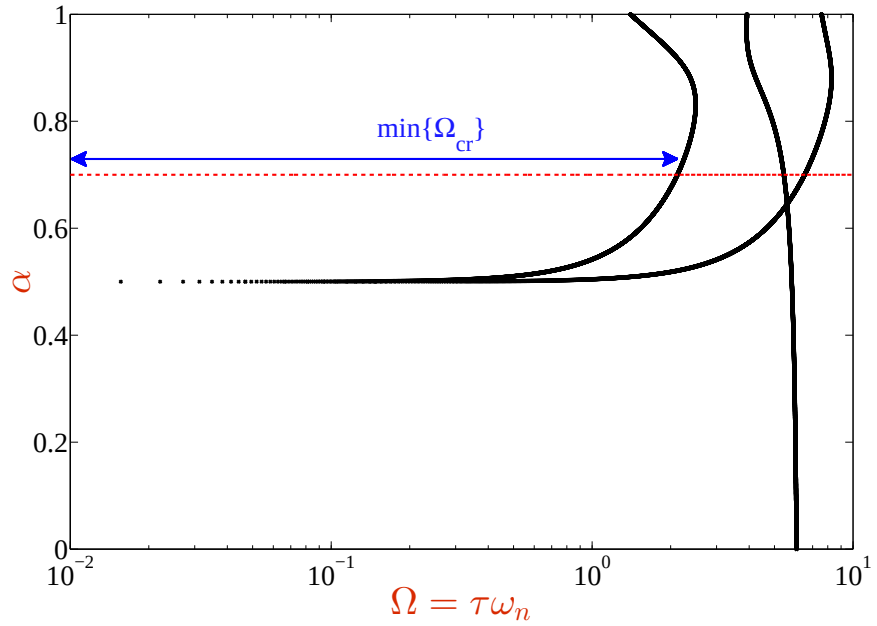

(a) Configuration 1: $\alpha = 0.7$, $\beta = 0.4$, $\gamma = 0.9$, $\zeta = 0.1$

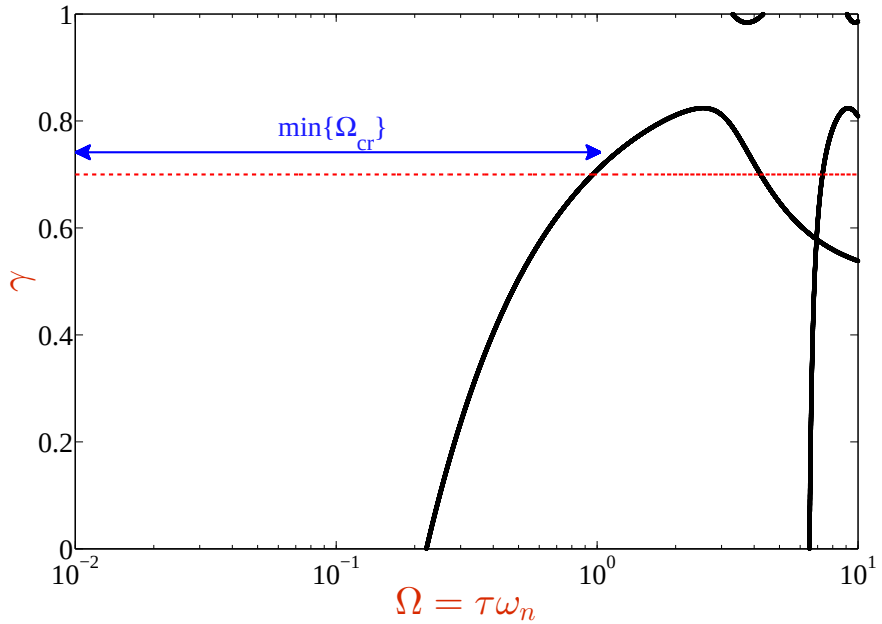

(b) Configuration 2: $\alpha = 0.9$, $\beta = 0.6$, $\gamma = 0.7$, $\zeta = 0.05$

Figure 2.3: Obtaining PSI using RTHS stability diagrams.

Table 2.2: Predictive stability indicators for different configurations.

	$\omega_n(rad/sec)$	$\Omega_{cr}(rad)$	PSI $(\log(msec))$
Configuration 1	3	2.123	6.56
Configuration 1	5	2.123	6.05
Configuration 1	10	2.123	5.36
Configuration 2	3	0.963	5.77
Configuration 2	5	0.963	5.26
Configuration 2	10	0.963	4.57

In Table 2.2, the PSI values associated with the two configurations shown in Fig. 2.3 and three natural frequencies are listed. As listed in Table 2.2, configuration 1 with $\omega_n = 3rad/sec$ and configuration 2 with $\omega_n = 10rad/sec$ lead to the largest PSI value (i.e. the largest margin of stability) and the lowest PSI value (i.e. the smallest margin of stability), respectively. It should be noted that the use of PSI becomes even more significant in implementation of multi-degree-of-freedom RTHS (or geographically distributed RTHS) because higher modes of the structure are highly sensitive to time delays and often suppressed with artificial damping in the numerical substructure.

2.1.3 Unconditionally Stable Region

As noted earlier, Eq. (2.17) may lead to 0, 1, or 2 meaningful critical frequency ratios. For case II and $\zeta = 5\%$, these three regions are shown in Fig. 2.4.

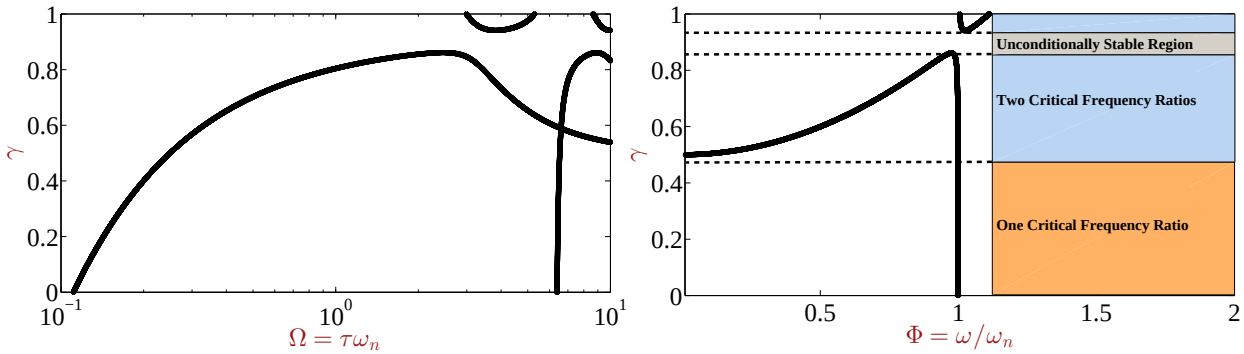

(a) Critical time delay

(b) Critical frequency ratio

Figure 2.4: Case II with $\zeta = 5\%$ a) Normalized RTHS stability diagram showing Ω_{cr} vs. γ b) Plot of ϕ_{cr} vs. γ showing the three stability regions.

Using Eq. (2.17), the required condition to have an unconditionally stable region is

$$(\gamma-\alpha)<4\zeta^2(1-2\beta)[(1-\alpha-\gamma)-(1-2\beta)\zeta^2]. \tag{2.21}$$

Moreover, in terms of α and γ, the range of the unconditionally stable region, which occurs about $\gamma-\alpha=0$, can be found using the following equation

$$(\gamma-\alpha)^2+B(\gamma-\alpha)+C=0 \tag{2.22}$$

where $B=4(1-2\beta)\zeta^2$ and $C=-4\zeta^2(1-2\beta)(1-2\alpha-(1-2\beta)\zeta^2)$. Using Eq. (2.22), the resulting unconditionally stable range associated with Case II about $\gamma-\alpha=0$ and associated with various damping ratios can be obtained, see Fig. 2.5.

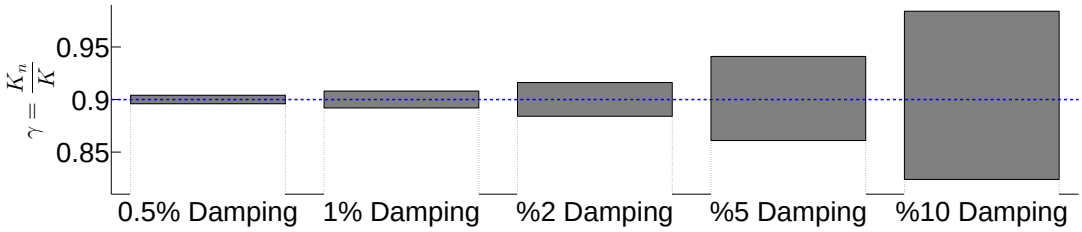

Figure 2.5: Unconditionally stable range associated with case II for different damping ratios.

Thus, in certain RTHS configurations, there is a range about $\gamma-\alpha=0$ in which the system is unconditionally stable, and within that range, the critical time delay and PSI approaches infinity. Knowing the unconditionally stable region associated with a partitioning setup can be significant, especially when conducting geographically-distributed RTHS where data loss and unpredictable time delays are major challenges.

2.1.4 Minimum Requirements of the Transfer System and Sampling Frequency

After obtaining the critical time delay using the RTHS stability diagrams or Eqs. (2.17) and (2.19a), one can identify the maximum permissible delay in an RTHS system as the critical time delay. Therefore, if the interaction force signal has a time delay equal to or greater than the critical time delay, the system will go unstable. Generally speaking, in SDOF RTHS, the time delay associated with the interaction force signal is

$$\tau_{F_{fb}} = \tau_{COMP} + \tau_{COMM} + \tau_{TS} \tag{2.23}$$

where τ_{COMP}, τ_{COMM}, and τ_{TS} are computational delay, communication delay, transfer system delay, respectively. Furthermore, if a ZOH digital-to-analog convertor is used, τ_{COMP} can be approximated by $(2f_s)^{-1}$ where f_s is the sampling frequency in Hz (Astrom and Wittenmark, 1990). Assuming that in a local RTHS, τ_{COMM} is a known deterministic value. Then, Eq. (2.23) becomes

$$\tau_{F_{fb}} - \tau_{COMM} - (2f_s)^{-1} = \tau_{TS}. \tag{2.24}$$

Therefore, with a given sampling frequency, the stability phase envelope which determines the minimum control requirements for the transfer system can be expressed as

$$e^{-j\omega(\tau_{cr}-\tau_{COMM}-(2f_s)^{-1})} = e^{-j\omega\tau_m} \tag{2.25}$$

where $\tau_m = \tau_{cr} - \tau_{COMM} - (2f_s)^{-1}$.

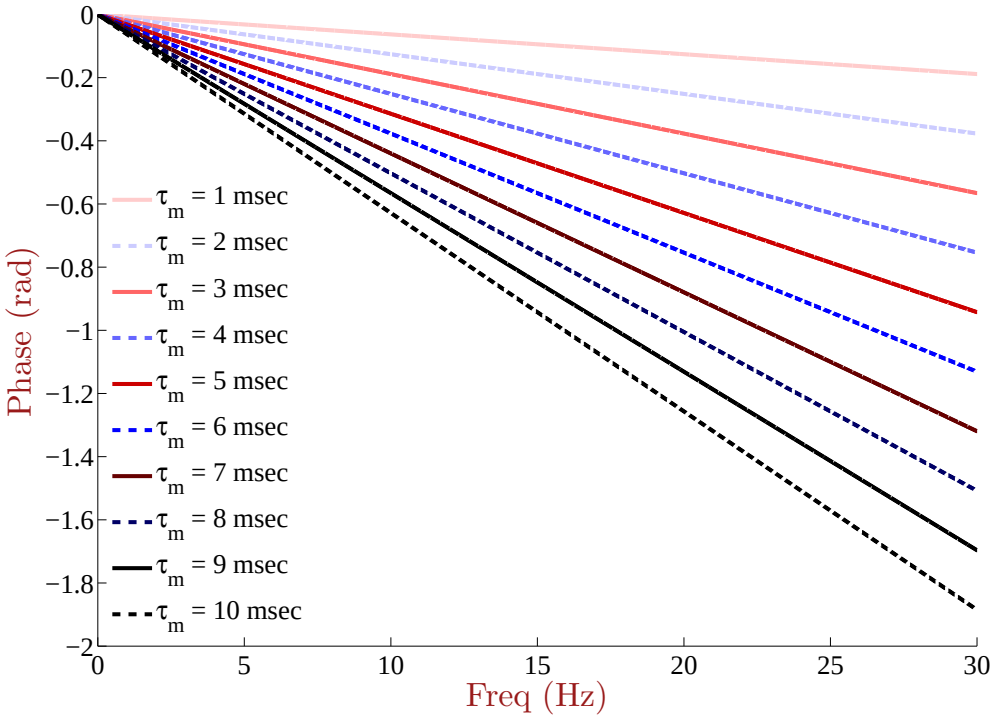

Figure 2.6: Stability phase envelope to determine the minimum transfer system control requirement.

As shown in Fig. 2.6, to conduct a stable SDOF RTHS, the phase plot of the transfer system control must lie above the stability phase envelope shown for a given value of τ_{cr}.

2.2 Weakly-Nonlinear SDOF RTHS Systems

This section considers a physical substructure that is composed of weakly-nonlinear materials, wherein there is a nonlinearity between the materials' restoring forces and displacements, or composed of linear materials but loaded beyond the proportional limit. Let's examine how nonlinearity affects the overall stability of a SDOF RTHS system in the presence of feedback time delay. Consider a lightly-damped reference structure with the governing equation

$$M\ddot{x}(t) + C\dot{x}(t) + Kx(t) + \zeta R(x) = 0 \tag{2.26}$$

which is equivalent to

$$\ddot{x}(t) + 2\zeta\omega_n\dot{x}(t) + {\omega_n}^2 x(t) + \zeta M^{-1} R(x) = 0 \tag{2.27}$$

where $\zeta R(x)$ represents the weakly-nonlinear component of the restoring force. Weakly-nonlinear systems can be divided into two categories, (1) strain-hardening and (2) strain-softening. Fig. 2.7 shows the qualitative behaviors of linear, strain-softening, and strain-hardening systems. In this work, we assume that these nonlinearities can be captured with cubic terms. Thus, Eq. (2.27) becomes

$$\ddot{x}(t) + 2\zeta\omega_n\dot{x}(t) + {\omega_n}^2 x(t) + \zeta M^{-1} h x^3(t) = 0 \tag{2.28}$$

where $\{h < 0, h = 0, h > 0\}$ corresponds to {strain-softening, linear, strain-hardening} systems. Eq. (2.28) can be partitioned into numerical and physical substructures using the partitioning parameters, $\{\alpha, \beta, \gamma\} = \{M_n/M, C_n/C, K_n/K\}$, yielding

$$\begin{aligned} &\{\alpha\ddot{x}(t) + 2\zeta\beta\omega_n\dot{x}(t) + \gamma{\omega_n}^2 x(t)\} \\ &+ \{(1-\alpha)\ddot{x}(t) + 2\zeta(1-\beta)\omega_n\dot{x}(t) + (1-\gamma){\omega_n}^2 x(t) + \zeta M^{-1} h x^3(t)\} = 0 \end{aligned} \tag{2.29}$$

where in the presence of feedback delay, Eq. (2.29) becomes

$$\begin{aligned} &\{\alpha\ddot{x}(t) + 2\zeta\beta\omega_n\dot{x}(t) + \gamma{\omega_n}^2 x(t)\} \\ &+ \{(1-\alpha)\ddot{x}(t-\tau) + 2\zeta(1-\beta)\omega_n\dot{x}(t-\tau) + (1-\gamma){\omega_n}^2 x(t-\tau)\} \\ &+ \{\zeta M^{-1} h x^3(t-\tau)\} = 0. \end{aligned} \tag{2.30}$$

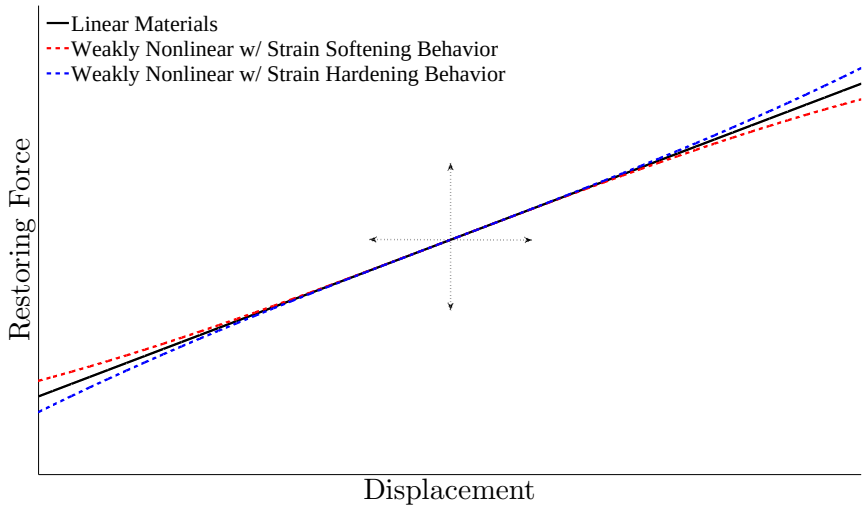

Figure 2.7: Qualitative behavior of linear strain-softening, and strain-hardening materials.

For a SDOF RTHS system, it has been shown that the presence of a feedback time delay effectively adds energy into the system (Ahmadizadeh, 2007; Mosqueda et al., 2005; Carrion and Spencer, 2007). Fig. 2.8 shows desired displacement against the restoring forces of linear and weakly-nonlinear systems associated with different time delays, where $\tau_1 < \tau_2 < \tau_3$. In each case, the additional energy added to the system is the enclosed area. Clearly, as the time delay becomes larger, the effective amount of added energy increases. For RTHS, instability occurs when the additional energy becomes greater than the energy dissipation in the nominal system (and hysteretic energy if any) (Ahmadizadeh, 2007). Using the stability switch criterion, we can obtain the critical time delay associated with the linear system, and the qualitative effects of weak nonlinearity on the stability of the system can be understood by computing and comparing the enclosed areas shown in Fig. 2.8.

Linear Systems

In Eq. (2.30), linear systems correspond to systems with $h = 0$. Therefore, the enclosed area in Fig. 2.8b, can be computed as

$$A_L(\tau) = \int_{x(t_0)}^{x(t_1)} (1-\gamma)K[x(t) - x(t-\tau)]dx \tag{2.31a}$$

$$A_L(\tau) = \int_{t_0}^{t_1} (1-\gamma)K[x(t) - x(t-\tau)]\dot{x}(t)dt. \tag{2.31b}$$

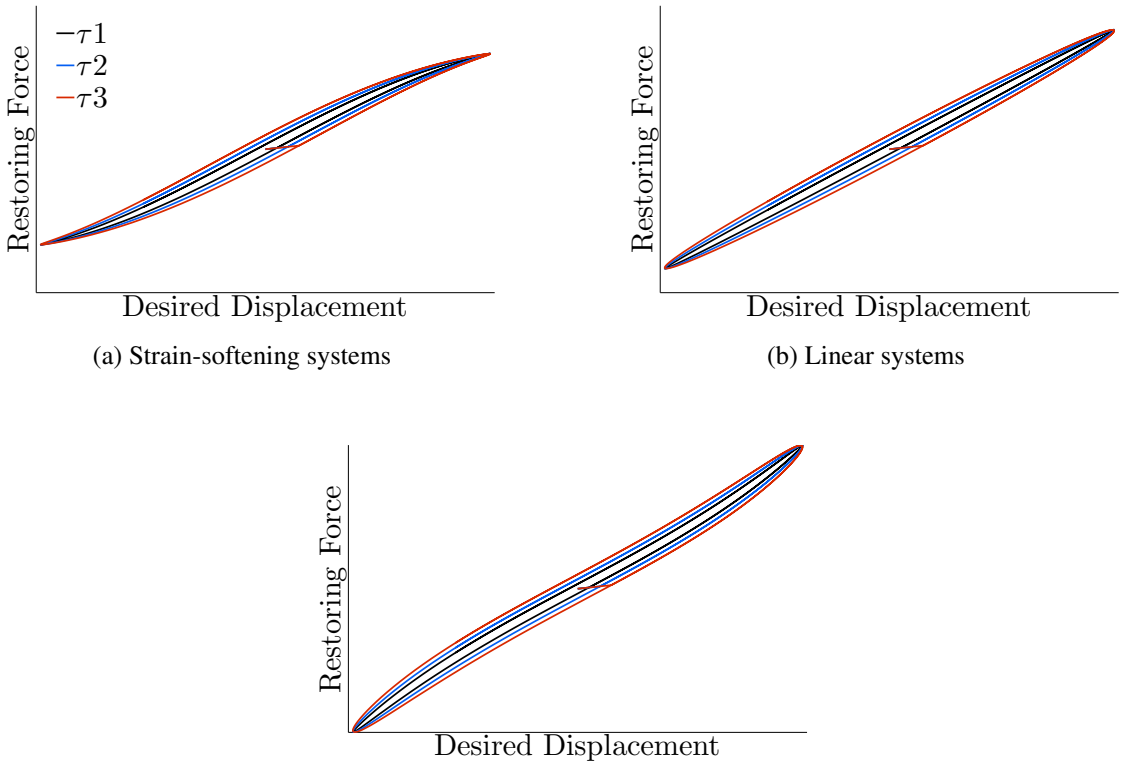

(a) Strain-softening systems

(b) Linear systems

(c) Strain-hardening systems

Figure 2.8: Additional energy due to time delay ($\tau_1 < \tau_2 < \tau_3$).

Strain-Softening Systems

In Eq. (2.30), strain-softening systems correspond to systems with $h<0$. Therefore, the enclosed area in Fig. 2.8a can be computed as

$$A_S(\tau) = \int_{x(t_0)}^{x(t_1)} \{(1-\gamma)K[x(t) - x(t-\tau)] + \zeta h[x^3(t) - x^3(t-\tau)]\}dx \tag{2.32a}$$

$$A_S(\tau) = \int_{t_0}^{t_1} [x(t) - x(t-\tau)]\{(1-\gamma)K + \zeta h[x^2(t) + x(t)x(t-\tau) + x^2(t-\tau)]\}\dot{x}(t)dt \tag{2.32b}$$

by applying the Tylor expansion on $[x(t) - x(t-\tau)]$ and truncating $o(\tau^2)$, $[x(t) - x(t-\tau)]$ can

be approximated as $[\tau\dot{x}(t)]$, yielding

$$A_S(\tau) \approx \int_{t_0}^{t_1} (1-\gamma)K[x(t)-x(t-\tau)]\dot{x}(t)dt + \int_{t_0}^{t_1} \zeta h\tau[x^2(t)+x(t)x(t-\tau)+x^2(t-\tau)]\dot{x}^2(t)dt \tag{2.32c}$$

$$A_S(\tau) \approx A_L(\tau) + \Delta A_S(\tau). \tag{2.32d}$$

Knowing that $\forall x(t), \tau$ and $\zeta h\tau < 0 : \zeta h\tau[x^2(t)+x(t)x(t-\tau)+x^2(t-\tau)]\dot{x}^2(t) \leq 0$ yields

$$\Delta A_S(\tau) \leq 0 \tag{2.33a}$$

$$A_S(\tau) \leq A_L(\tau). \tag{2.33b}$$

Thus, the enclosed area in Fig. 2.8a (i.e. the additional energy for strain-softening systems) is always smaller than the enclosed area in Fig. 2.8b (i.e. the additional energy for linear systems).

Strain-Hardening Systems

In Eq. (2.30), strain-hardening systems correspond to systems with $h>0$. Therefore, the enclosed area in Fig. 2.8c can be computed as

$$A_H(\tau) = \int_{x(t_0)}^{x(t_1)} \{(1-\gamma)K[x(t)-x(t-\tau)] + \zeta h[x^3(t)-x^3(t-\tau)]\}dx \tag{2.34a}$$

$$A_H(\tau) = \int_{t_0}^{t_1} [x(t)-x(t-\tau)]\{(1-\gamma)K + \zeta h[x^2(t)+x(t)x(t-\tau)+x^2(t-\tau)]\}\dot{x}(t)dt$$

by applying the Tylor expansion on $[x(t)-x(t-\tau)]$ and truncating $o(\tau^2)$, $[x(t)-x(t-\tau)]$ can be approximated as $[\tau\dot{x}(t)]$, yielding

$$A_H(\tau) \approx \int_{t_0}^{t_1} (1-\gamma)K[x(t)-x(t-\tau)]\dot{x}(t)dt + \int_{t_0}^{t_1} \zeta h\tau[x^2(t)+x(t)x(t-\tau)+x^2(t-\tau)]\dot{x}^2(t)dt \tag{2.34b}$$

$$A_H(\tau) \approx A_L(\tau) + \Delta A_H(\tau). \tag{2.34c}$$

Knowing that $\forall x(t), \tau$ and $\zeta h\tau > 0 : \zeta h\tau[x^2(t)+x(t)x(t-\tau)+x^2(t-\tau)]\dot{x}^2(t) \geq 0$ yields

$$\Delta A_H(\tau) \geq 0 \tag{2.35a}$$

$$A_H(\tau) \geq A_L(\tau). \tag{2.35b}$$

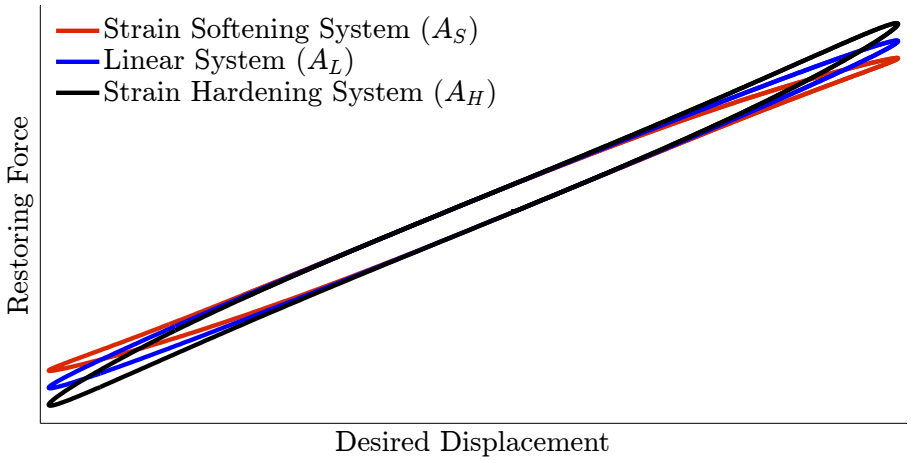

Figure 2.9: Additional energy added to the system due to time delay in the restoring force.

Thus, the enclosed area in Fig. 2.8c (i.e. the additional energy for strain-hardening systems) is always larger than the enclosed area in Fig. 2.8b (i.e. the additional energy for linear systems). In Fig. 2.9, for a given τ, $A_S(\tau), A_L(\tau)$, and $A_H(\tau)$ are compared, and clearly

$$A_H(\tau) \geq A_L(\tau) \geq A_S(\tau). \tag{2.36}$$

For weakly-nonlinear systems, the system can be linearized about its fixed point and using the RTHS stability switch criterion, a value for critical time delay can be obtained. However, it should be noted that depending upon whether the system exhibits softening or hardening behavior, the obtained value is underestimated or overestimated, respectively. Therefore, for weakly-nonlinear systems with softening behavior, the obtained value is a conservative value. Furthermore, $A_L(\tau) - A_S(\tau)$ and $A_H(\tau) - A_L(\tau)$ are linearly proportional to $\zeta h\tau$. Thus, the level of nonlinearity and damping of the reference structure determine the level of overestimation or underestimation of the critical time delay value obtained using the RTHS stability switch criterion.

Chapter 3

Performance

In this chapter, the objective is to propose a new performance indicator, the predictive performance indicator (PPI), to predict the performance of an RTHS system prior to its implementation. Thus, the PPI belongs to the first category of RTHS indicators (i.e. pre-experiment indicators). In this category, indicators are computed prior to an experiment (pre-experiment) to enable a researcher to predict the susceptibility of an RTHS configuration to any systematic or random sources of error. The PPI assesses how transfer system dynamics and computational/communication delays, which are the significant sources of systematic experimental error in RTHS, distort RTHS responses and how the corresponding error propagates through the entire RTHS. This indicator is developed in a way to be reconcilable with the RTHS stability switch criterion.

3.1 Impact of Delay on Modal Characteristics

It has been shown that when a time delay is present in the system, the effect of that delay is similar to that of negative damping. The concept of effective damping was first applied to RTHS in (Horiuchi et al., 1996, 1999). This interpretation of the impact of time delay has been used by several other researchers as well, for example see (Mosqueda et al., 2007a; Ahmadizadeh, 2007; Gao, 2012). For instance, Mosqueda, *et al.* considered the following partitioning of a SDOF linear system

$$M\ddot{x}(t) + C\dot{x}(t) = -M\ddot{x}_g(t) - F_{fb}(t-\tau) \tag{3.1a}$$

$$F_{fb}(t) = Kx(t). \tag{3.1b}$$

To investigate the impact of time delay in this system, they compared the dynamics of the delay frequency response and the frequency response of the reference system and showed that this SDOF

RTHS system can be approximated as

$$M\ddot{x}(t) + C'\dot{x}(t) + Kx = -M\ddot{x}_g(t) \tag{3.2}$$

where $C' = 2\zeta_{eff}\omega_n$ and ζ_{eff} is a function of damping ratio (ζ), natural frequency of the reference structure (ω_n), and time delay (τ). Mosqueda, *et al.* showed that

$$\zeta_{eff} = \sqrt{\zeta^2 - \zeta\sin(\tau\omega_n) + \frac{1-\cos(\tau\omega_n)}{2}}. \tag{3.3}$$

It should be noted that in the derivation of Eq. (3.3), they assumed that the resonant peaks of the reference structure and the RTHS system occur at the same frequency. Eq. (3.3) provides an effective damping corresponding to a particular partitioning configuration shown in Eqs. (3.1a) and (3.1b).

Let's systematically consider the impact of system partitioning in a general partitioning configuration by utilizing the three parameters, $\alpha = M_n/M$, $\beta = C_n/C$, and $\gamma = K_n/K$. Consider the SDOF RTHS system, Eqs. (2.2a) and (2.2b), and divide them by M, yielding

$$\{\alpha\ddot{x}(t)+2\beta\zeta\omega_n\dot{x}(t)+\gamma{\omega_n}^2x\}+\{(1-\alpha)\ddot{x}(t)+2(1-\beta)\zeta\omega_n\dot{x}(t)+(1-\gamma){\omega_n}^2x\} = -\ddot{x}_g(t). \tag{3.4}$$

With a Fourier transform of Eq. (3.4), the frequency response function of the partitioned system, $x(j\omega)$ is obtained as

$$x(j\omega) = \frac{-1}{{\omega_n}^2C_N + {\omega_n}^2C_Pe^{-j\tau\omega}}\ddot{x}_g(j\omega) \tag{3.5}$$

where

$$C_N = -\alpha(\omega/\omega_n)^2 + j2\beta\zeta(\omega/\omega_n) + \gamma \tag{3.6a}$$

$$C_P = -(1-\alpha)(\omega/\omega_n)^2 + j2(1-\beta)\zeta(\omega/\omega_n) + (1-\gamma). \tag{3.6b}$$

Eq. (3.5) can be normalized with respect to ω_n, as

$$\omega_n^2x(j\omega) = \frac{-1}{C_N + C_Pe^{-j\tau\omega}}\ddot{x}_g(j\omega). \tag{3.7}$$

Using the values introduced in the preceding chapter, $\phi = \omega/\omega_n$ and $\Omega = \tau\omega_n$, Eqs. (3.6a) and (3.6b) can be written as

$$C_N = -\alpha\phi^2 + j2\beta\zeta\phi + \gamma \tag{3.8a}$$

$$C_P = -(1-\alpha)\phi^2 + j2(1-\beta)\zeta\phi + (1-\gamma). \tag{3.8b}$$

Furthermore,

$$e^{-j\tau\omega} = e^{-j\Omega\phi} \tag{3.9}$$

and the normalized characteristic equation of the SDOF RTHS in Eq. (3.4) becomes

$$\begin{aligned}\Gamma(\phi,\Omega) = \{(-\alpha\phi^2+\gamma) + [(\alpha-1)\phi^2 + (1-\gamma)]\cos(\Omega\phi) + (2\zeta(1-\beta)\phi)\sin(\Omega\phi)\} \\ +\{(2\zeta\beta\phi) + [2\zeta(1-\beta)\phi]\cos(\Omega\phi) + [(1-\alpha)\phi^2 - (1-\gamma)]\sin(\Omega\phi)\}j\end{aligned} \tag{3.10}$$

where the normalized characteristic equation of the reference structure in Eq. (2.1) can be expressed as

$$\Gamma(\phi) = -\phi^2 + j2\zeta\phi + 1. \tag{3.11}$$

By comparing the roots of Eq. (3.10) and Eq. (3.11), a SDOF RTHS shown in Eq. (3.4) can be approximated as

$$\ddot{x}(t) + 2\zeta_{eff}\omega_n\dot{x}(t) + {\omega_n}^2 x = -\ddot{x}_g(t) \tag{3.12}$$

where, the effective damping becomes

$$\zeta_{eff} = \sqrt{A_0 + A_1\zeta + A_2\zeta^2} \tag{3.13}$$

and

$$\begin{aligned}A_0 &= 0.5(\gamma-\alpha)^2(1-cos(\Omega)) \\ A_1 &= \sin(\Omega)(\gamma-\alpha) \\ A_2 &= 1 + 2\beta(1-\cos(\Omega))(\beta-1).\end{aligned} \tag{3.14}$$

It should be noted that in the derivation of Eq. (3.13), the assumption is that the resonant peak in Eq. (3.5) occurs in the close vicinity of ω_n meaning that the presence of delay in the feedback force signal does not affect the value of natural frequency (ω_n) significantly.

3.2 Predictive Performance Indicator (PPI)

In this section, we use the frequency response function of error in SDOF RTHS due to time delay, to establish a new performance metric. The proposed metric is a function of the steady state variance of error subject to band-limited white noise and natural frequency of the reference structure (ω_n). The frequency response function of the reference structure in Eq. (2.1) can be expressed as

$$x_{REF}(j\omega) = \frac{-\ddot{x}_g(j\omega)}{-\omega^2 + 2j\zeta\omega_n\omega + {\omega_n}^2}. \tag{3.15}$$

Eq. (3.15) can be normalized with respect to ω_n as follows

$$x_{REF}(j\phi) = \frac{-1}{{\omega_n}^2 C_R}\ddot{x}_g(j\phi) \tag{3.16}$$

where

$$C_R = -(\omega/\omega_n)^2 + 2j\zeta\omega/\omega_n + 1 = -\phi^2 + 2j\zeta\phi + 1. \tag{3.17}$$

From Eq. (3.5), the normalized frequency response function of SDOF RTHS can be expressed as

$$x_{RTHS}(j\phi, \Omega) = \frac{-1}{{\omega_n}^2[C_N + C_P e^{-j\Omega\phi}]}\ddot{x}_g(j\phi). \tag{3.18}$$

Here, it should be noted that in the absence of a feedback time delay, the frequency response of RTHS, $x_{RTHS}(j\phi, \Omega)$, and that of the reference structure, $x_{REF}(j\phi)$, are identical. For $\tau = 0$ (i.e. $\Omega = \tau\omega_n = 0$), $e^{j\Omega\phi}$ becomes 1. Therefore,

$$x_{REF}(j\phi) = x_{RTHS}(j\phi, 0) = \frac{-1}{{\omega_n}^2[C_N + C_P \times 1]}\ddot{x}_g(j\phi) = \frac{-1}{{\omega_n}^2 C_R}\ddot{x}_g(j\phi). \tag{3.19}$$

However, for $\tau \neq 0$, the frequency response function of the error due to the presence of time delay in the feedback force signal can be expressed as

$$H_{ERR}(\Omega, \phi) = \frac{x_{REF}(j\phi) - x_{RTHS}(j\phi, \Omega)}{\ddot{x}_g(j\phi)} = \frac{C_P(1 - e^{-j\Omega\phi})}{\omega_n^2 C_R(C_N + C_P e^{-j\Omega\phi})}. \tag{3.20}$$

The autospectral density of the error is

$$S_{ERR}(\Omega, \phi) = S_g(\phi)|H_{ERR}(\Omega, \phi)|^2 = S_g(\phi)H_{ERR}(\Omega, \phi)H^*_{ERR}(\Omega, \phi) \tag{3.21}$$

where $\{\ldots\}^*$ and S_g represent the complex conjugate of $\{\ldots\}$ and autospectral density (or power spectral density) of the ground acceleration, respectively. It should be noted that S_g is frequency-dependent for eqrthquake histories and constant for white noise ground accelerations. The steady-state variance of the error is related to the autospectral density as follows

$$\sigma^2 = \lim_{r' \to \infty} \frac{1}{2\pi} \int_{-r'}^{r'} S_{ERR}(\omega)\, \mathrm{d}\omega. \tag{3.22}$$

Next, we introduce a new variable I_{ERR}, defined as

$$I_{ERR} = \omega_n^2 H_{ERR} = \frac{C_P(1 - e^{-j\Omega\phi})}{C_R(C_N + C_P e^{-j\Omega\phi})}. \tag{3.23}$$

Thus, using Eqs. (3.21) - (3.23), the steady-state variance of the error presented in a stationary SDOF RTHS becomes

$$\sigma^2 = \lim_{r'\to\infty} \frac{1}{2\pi} \int_{-r'}^{r'} S_g |H_{ERR}|^2 \, \mathrm{d}\omega \; = \lim_{r'\to\infty} \frac{1}{2\pi\omega_n^4} \int_{-r'}^{r'} S_g |I_{ERR}|^2 \, \mathrm{d}\omega. \tag{3.24}$$

With a change of variable, Eq. (3.24) becomes

$$\sigma^2 = \lim_{r\to\infty} \frac{1}{2\pi\omega_n^3} \int_{-r}^{r} S_g |I_{ERR}|^2 \, \mathrm{d}\phi \tag{3.25}$$

where $r = r'/\omega_n$. Taking advantages of the symmetry of autospectral density and constant autospectral density of white noise ground acceleration input, we propose a performance metric, predictive performance indicator (PPI), as

$$PPI = \lim_{r\to\infty} \frac{1}{\pi} \int_{0}^{r} |I_{ERR}|^2 \, \mathrm{d}\phi \; = \omega_n^3 \sigma^2 S_g^{-1}. \tag{3.26}$$

Eq. (3.26) indicates that the steady-state variance of the error can be found by computing the area under the normalized autospectral density function of the error. Usually, the peak of $|I_{ERR}|^2(\pi)^{-1}$ occurs at $\phi \approx 1$ which corresponds to $\omega \approx \omega_n$ and the frequency bandwidth of interest is the seismic frequency bandwidth and it is restricted to a low frequency bandwidth ($0 < \omega < \omega_s$). Therefore, as shown in Fig. 3.1, for $r \approx \omega_s/\omega_n$, $\omega_n^3\sigma^2/S_g$ is approximated as

$$PPI = \frac{1}{\pi} \int_{0}^{r} |I_{ERR}|^2 \, \mathrm{d}\phi \; \approx \omega_n^3 \sigma^2 / S_g. \tag{3.27}$$

To derive the PPI in Eq. (3.26), we chose delta-correlated white noise ground acceleration with a constant autospectral density (S_g) over the whole spectrum. However, it should be noted that, for any specific seismic record, a similar indicator can be produced using the following equation

$$PPI' = \frac{1}{2\pi} \frac{\int_0^{r'\omega_n^{-1}} S_g(\phi) |I_{ERR}|^2 \, \mathrm{d}\phi}{\int_0^{r'\omega_n^{-1}} S_g(\phi) \, \mathrm{d}\phi} \approx \omega_n^3 \sigma^2 [\int_0^{r'\omega_n^{-1}} S_g(\phi) \, \mathrm{d}\phi]^{-1} \tag{3.28}$$

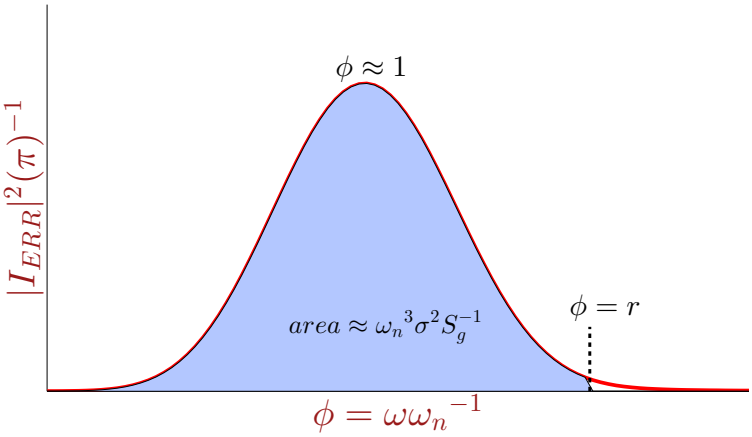

Figure 3.1: PPI is the area under the normalized autospectral density function.

where S_g' is the frequency-dependent auto-spectral density of the seismic input and $[0, r']$ is the corresponding seismic bandwidth.

3.2.1 Performance Diagrams for a Linear SDOF RTHS

In this section, we illustrate how the values of the partitioning parameters, transfer system performance, and the structural characteristics of the reference structure affect the performance of a linear RTHS system using the proposed metric, the PPI. Varying four different parameters (α, β, γ, and ζ), nine different partitioning cases, listed in Table 3.1, are considered and the corresponding PPI values are plotted in Fig. 3.2. Furthermore, using the RTHS stability switch criterion, (Maghareh et al., 2013), the stability diagrams associated with each partitioning case are plotted. It should be noted that a lower PPI indicates more reliability of the RTHS results. Clearly, this performance analysis is only valid for the stable region that is the area to the left of the stability switch curve ($\Omega < \Omega_{cr}$).

Table 3.1: Partitioning parameters of the nine cases examined

	Case 1	Case 2	Case 3	Case 4	Case 5	Case 6	Case 7	Case 8	Case 9
α	$\in [0,1]$	0.8	0.95	$\in [0,1]$	0.8	0.8	$\in [0,1]$	0.8	$\in [0,1]$
β	0.5	0.5	0.5	0.5	0.5	$\in [0,1]$	0.5	0.5	0.5
γ	0.1	$\in [0,1]$	$\in [0,1]$	0.1	$\in [0,1]$	0.1	0.1	$\in [0,1]$	0.25
ζ	0.01	0.01	0.01	0.02	0.02	0.02	0.04	0.04	0.04

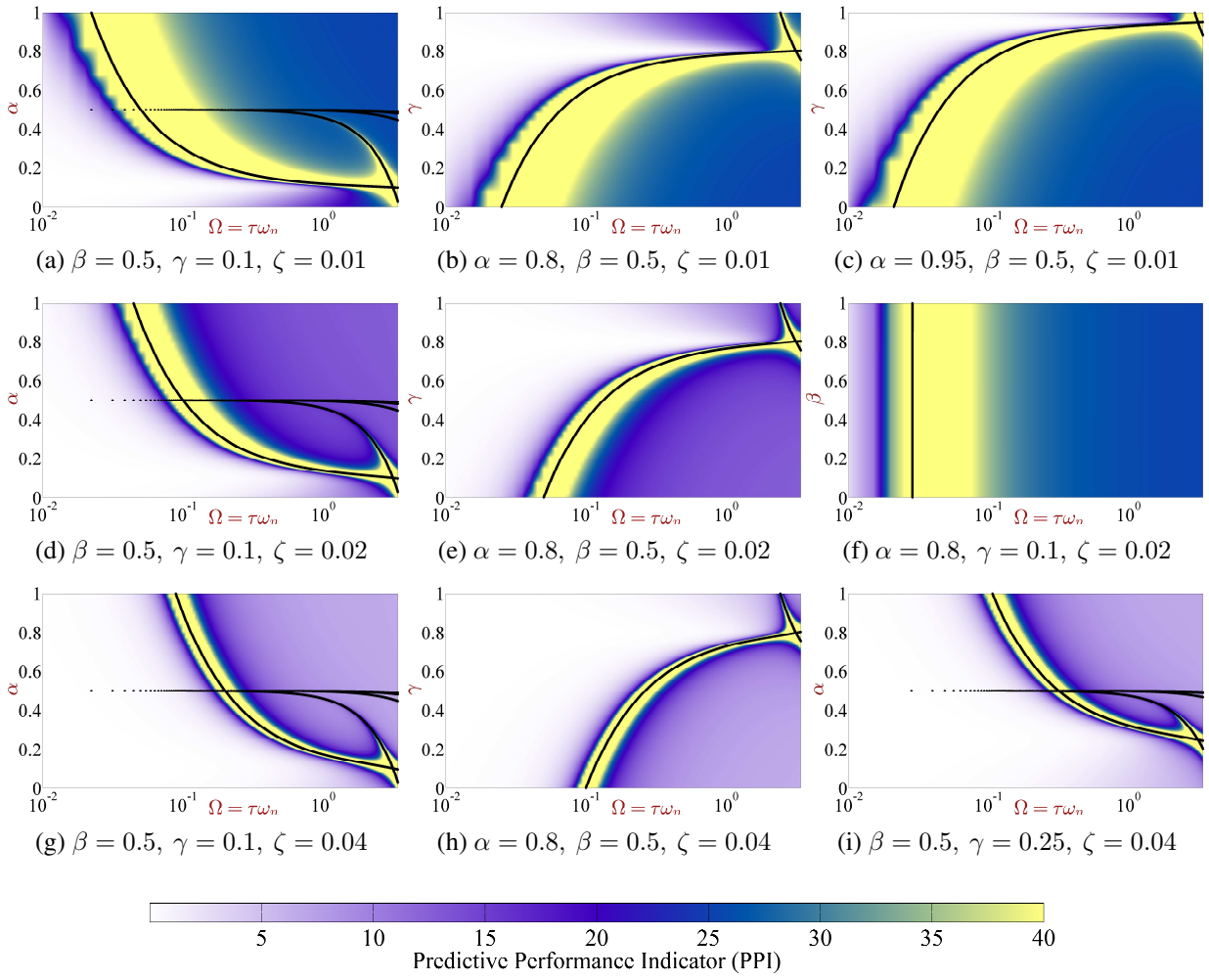

Figure 3.2: Performance/stability diagrams of the nine cases listed in Table 3.1.

Some important observations can be made from Fig. 3.2.

- As a rule of thumb, the PPI is closely related to the value of $|\gamma - \alpha|$. For a specific transfer system performance, designing an experiment to have a smaller value of $|\gamma - \alpha|$ usually leads to a lower PPI and better performance.

- For a specific transfer system performance, a reference structure with a higher damping leads to a more successful simulation. To see the impact of the reference structure's damping (ζ), one can compare Figs. 3.2a, 3.2d, and 3.2g or Figs. 3.2b, 3.2e, and 3.2h.

- The overall success of an RTHS is almost independent of how the reference structure's damping is partitioned (β factor) between the numerical and physical substructures, see Fig. 3.2f.

- To achieve a better performance in conducting SDOF RTHS with a specific transfer system, decreasing $|\gamma - \alpha|$, ω_n and/or increasing ζ are effective options.
- To conduct a successful RTHS, the partitioning configuration needs to be sufficiently away from the stability switch curve.
- Generally speaking, conducting an RTHS with a small value of γ (i.e. more stiffness in the physical substructure) and a large value of α (i.e. more mass in the numerical substructure) is the most challenging configuration, see Figs. 3.2a, 3.2b, 3.2c, and 3.2f.

Chapter 4

Illustrative Examples

To illustrate the utility of the PSI and PPI, we have provided three different types of examples, virtual RTHS with pure time delay, virtual RTHS with time delay and transfer system dynamics, and an actual RTHS example. Herein, virtual RTHS (vRTHS) referes to performing RTHS on a real-time virtual platform (e.g. xPC target and dSPACE) where the physical substructure(s), transfer system, and communication system are all modeled numerically to mimic a real-time virtual simulation of the RTHS itself.

4.1 Virtual RTHS with Pure Time Delay

A simple way to conduct vRTHS is to lumpt the transfer system dynamics, communication and computational delays are all lumped into a single time delay (τ), see Fig. 4.1.

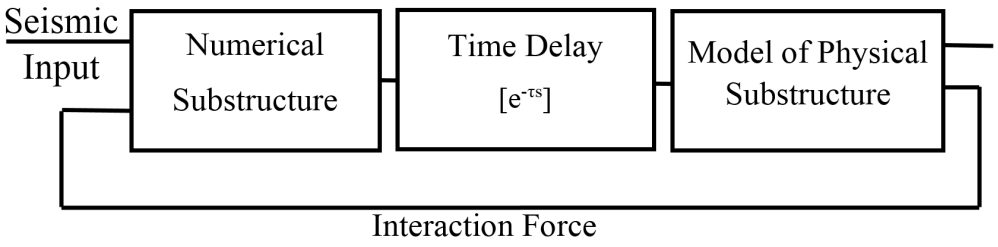

Figure 4.1: Virtual RTHS with pure time delay.

In this section, the results of 2000 realizations of vRTHS(s) with pure time delay are shown to verify that, (1) the PPI is independent of the power of the input ground acceleration and (2) the PPI is a function of the value of $\Omega = \tau\omega_n$ and not the value of τ or ω_n, independently. Furthermore,

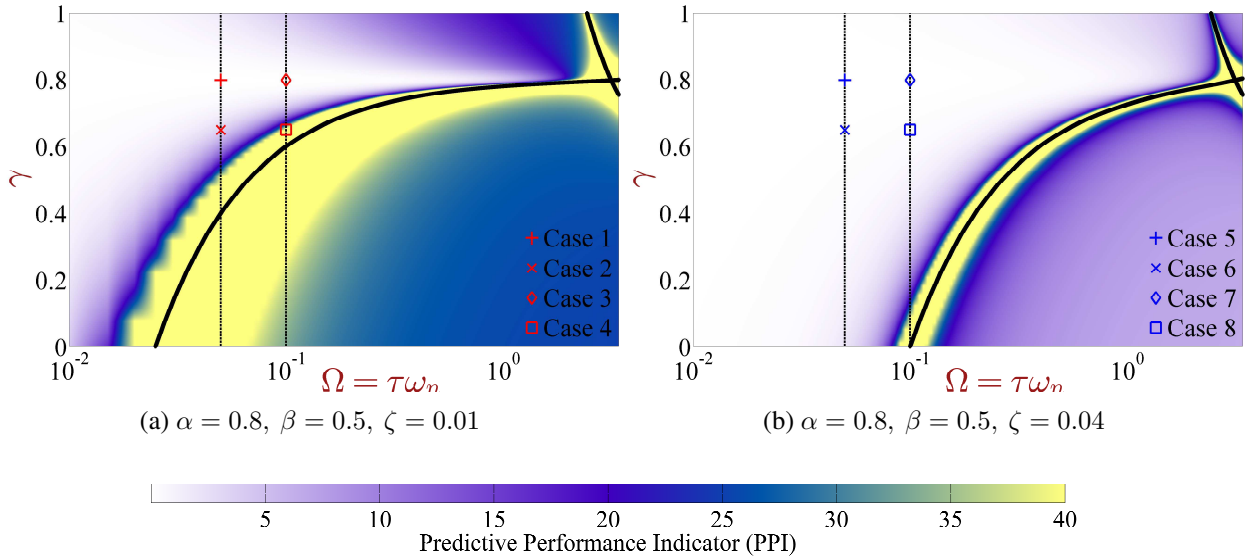

(a) $\alpha = 0.8,\ \beta = 0.5,\ \zeta = 0.01$ (b) $\alpha = 0.8,\ \beta = 0.5,\ \zeta = 0.04$

Figure 4.2: Indication of vRTHS cases on the performance/stability diagrams.

the impact of $|\gamma - \alpha|$, ζ, and Ω, which are the most influential parameters on the PPI, is investigated. In this study, eight different cases, listed in Table 4.1, are selected and each case is virtually simulated in MATLAB using 125 different values of τ and two band-limited white noise inputs (with autospectral density of $S_g = 1\ m^2sec^2$ and $S_g = 2\ m^2sec^2$). So, a total of 2000 vRTHS are conducted ($8 \times 2 \times 125$). In Fig. 4.2, these eight cases are indicated on the performance diagrams.

Table 4.1: Simulation case studies ($\alpha = 0.8$ and $\beta = 0.5$)

	γ	ζ	Ω	PPI
Case 1	0.8	0.01	0.05	9.1×10^{-3}
Case 2	0.65	0.01	0.05	3.5×10^{0}
Case 3	0.8	0.01	0.1	3.6×10^{-2}
Case 4	0.65	0.01	0.1	5.1×10^{1}

	γ	ζ	Ω	PPI
Case 5	0.8	0.04	0.05	2.3×10^{-3}
Case 6	0.65	0.04	0.05	3.4×10^{-2}
Case 7	0.8	0.04	0.1	9.1×10^{-3}
Case 8	0.65	0.04	0.1	1.6×10^{-1}

In Fig. 4.3, the $\omega_n^3\sigma^2/S_g$ values obtained from the vRTHS results are compared with the corresponding PPI values using Eq. (3.27). Each subfigure shows two sets of results corresponding to the two input ground accelerations. Some important observations can be made from Fig. 4.3.

- PPI is independent of the power of the input ground acceleration. As one can see in Figs. 4.3a-4.3h, the PPI values are independent of which input ground acceleration is chosen.

- In each subfigure, the value of $\Omega = \tau\omega_n$ is constant, yet, τ and ω_n vary dependently (i.e.

$\tau = \Omega/\omega_n$). The results indicate that the PPI is a function of the value of Ω and not the value of τ or ω_n, independently.

- A smaller values of $|\gamma - \alpha|$ and ω_n leads to a smaller PPI which corresponds to a more successful RTHS.
- A larger value of ζ leads to a smaller PPI value which corresponds to a more successful RTHS.

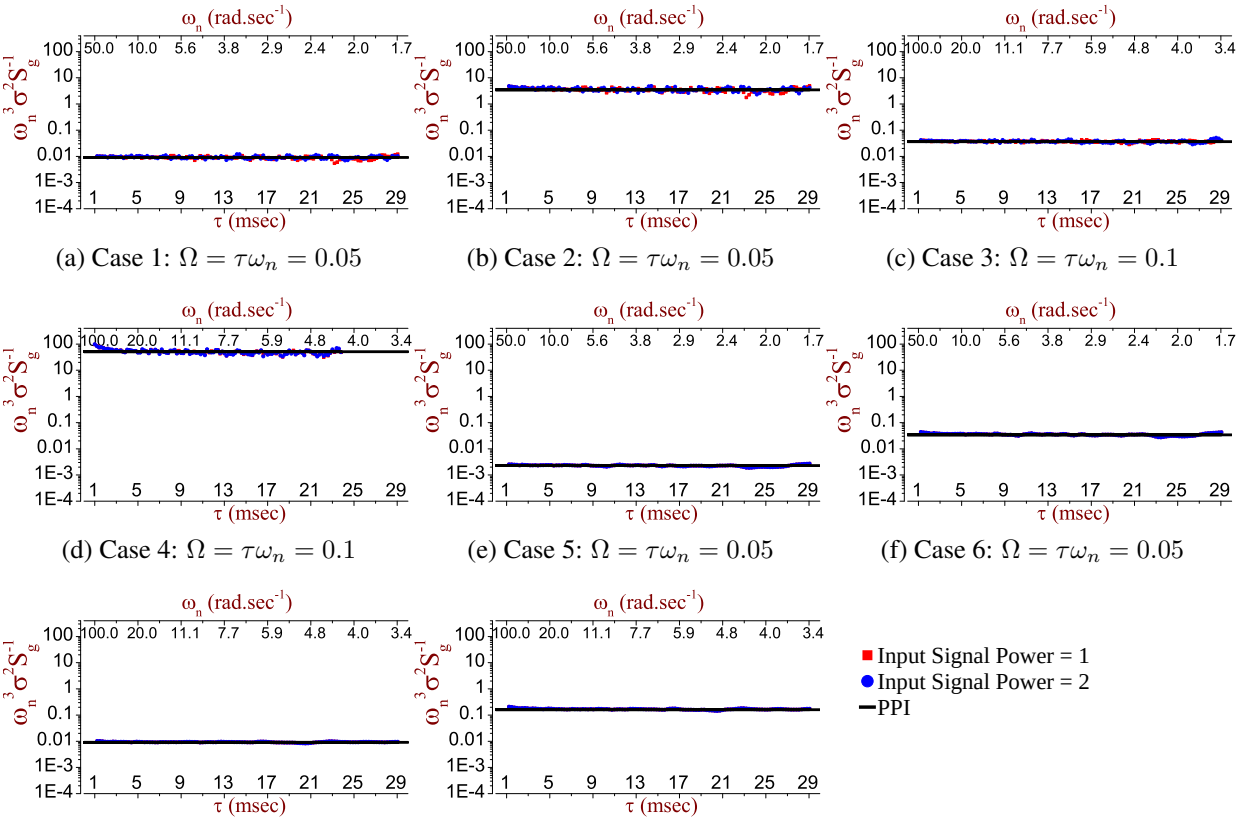

(a) Case 1: $\Omega = \tau\omega_n = 0.05$ (b) Case 2: $\Omega = \tau\omega_n = 0.05$ (c) Case 3: $\Omega = \tau\omega_n = 0.1$

(d) Case 4: $\Omega = \tau\omega_n = 0.1$ (e) Case 5: $\Omega = \tau\omega_n = 0.05$ (f) Case 6: $\Omega = \tau\omega_n = 0.05$

(g) Case 7: $\Omega = \tau\omega_n = 0.1$ (h) Case 8: $\Omega = \tau\omega_n = 0.1$

Figure 4.3: Comparisons of the simulated values of $\omega_n^3\sigma^2 S_g^{-1}$ associated with various partitioning choices with the corresponding PPI values.

4.2 Virtual RTHS with Transfer System Dynamics

In this section, to conduct a more realistic vRTHS, actual transfer system dynamics are embedded in vRTHS, see Fig. 4.4. Therefore, two controlled servo-hydraulic actuators were identified at the

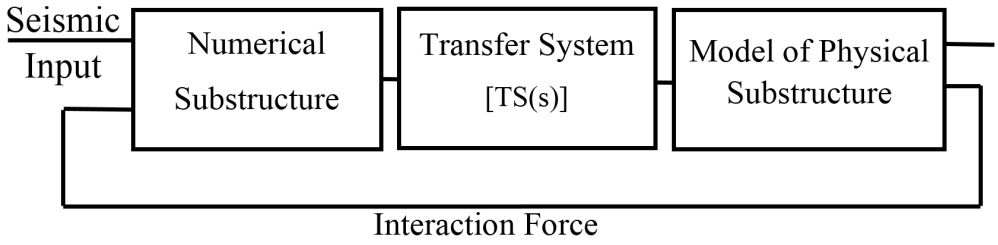

Figure 4.4: Virtual RTHS with transfer system dynamics.

Intelligent Infrastructure System Lab (*IISL*) at Purdue University. The identified dynamics of the two servo-hydraulic actuators (i.e. command displacement to measured displacement) are,

$$TS_1 = \frac{x_{msd}(\omega)}{x_{cmd}(\omega)} = \frac{2.382 \times 10^9}{\omega^4 - j485.5\omega^3 - 1.317 \times 10^5\omega^2 + j3.182 \times 10^7\omega + 2.382 \times 10^9} \tag{4.1}$$

$$TS_2 = \frac{x_{msd}(\omega)}{x_{cmd}(\omega)} = \frac{4.520 \times 10^9}{\omega^4 - j577.1\omega^3 - 2.680 \times 10^5\omega^2 + j6.282 \times 10^7\omega + 4.930 \times 10^9} \tag{4.2}$$

and, the corresponding magnitude and phase plots are as follows.

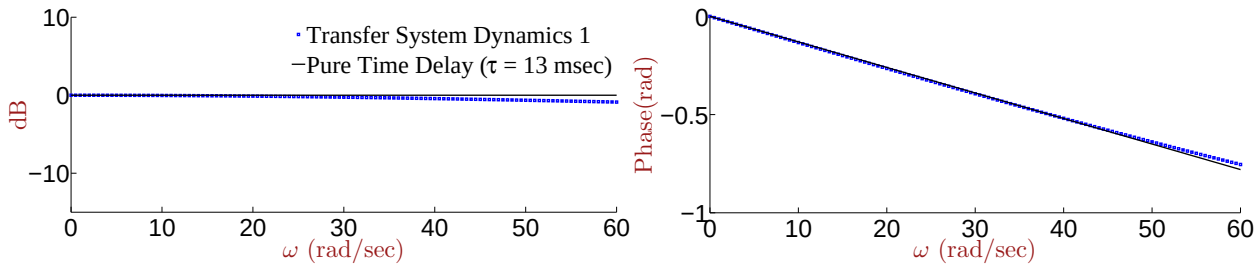

(a) Magnitude plot (b) Phase plot

Figure 4.5: Frequency responses of the hydraulic actuator (TS_1) and a pure time delay system.

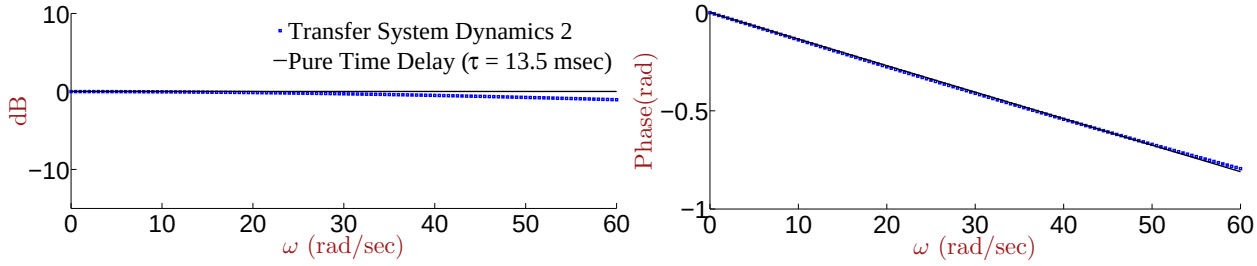

(a) Magnitude plot (b) Phase plot

Figure 4.6: Frequency responses of the hydraulic actuator (TS_2) and a pure time delay system.

In this study, 198 vRTHS(s) listed in Table 4.2 were conducted in which the input is a band-

limited white noise with the Gaussian distribution (signal power = 1) and natural frequency of the reference structure (ω_n) is the variable. In the first set of vRTHS, 99 vRTHS(s) are conducted with the partitioning choice No.1 and the transfer system 1 (TS_1). In the second set of vRTHS, 99 vRTHS(s) are conducted with the partitioning choice No.2 and the transfer system 2 (TS_2).

Table 4.2: Partitioning choices

Choice No.	α	β	γ	ζ	Computational Delay	Communication Delay
1	0.8	0.5	0.8	0.01	8192^{-1}	4096^{-1}
2	0.9	0.5	0.9	0.02	2048^{-1}	1024^{-1}

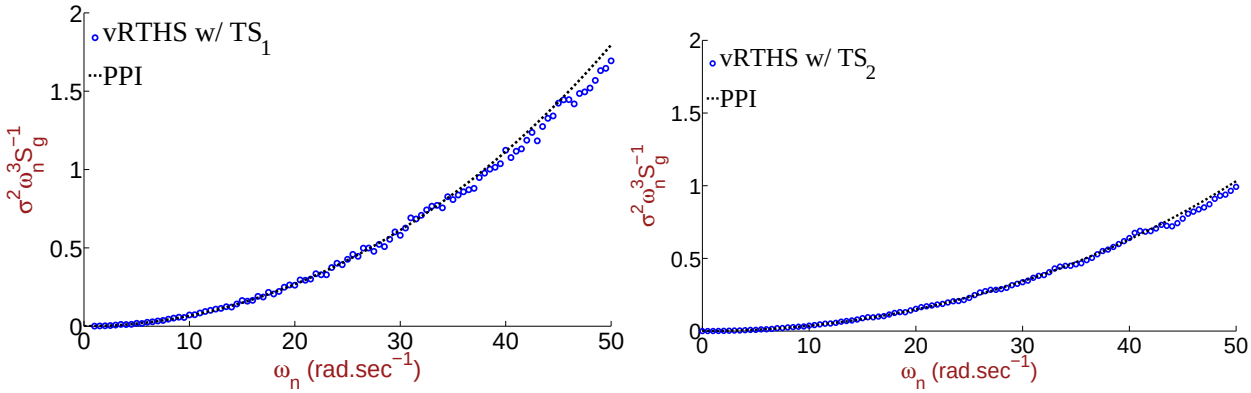

(a) vRTHS with TS_1 (b) vRTHS with TS_2

Figure 4.7: Comparisons of the $\sigma^2\omega_n^3 S_g^{-1}$ values obtained from vRTHS(s) with the corresponding PPI values.

In Fig. 4.7, the $\sigma^2\omega_n^2/S_g$ values resulting in the vRTHS(s) are compared with the corresponding PPI. The comparisons show that the PPI can be also effectively used when transfer system dynamics (not transfer system delay), computational delays, and communication delays are all considered in vRTHS.

4.3 An RTHS Case Study

In this section, we conduct a pure physical (shake table) testing of a SDOF structure (i.e. the reference structure), a simulation of the reference structure (i.e. reference model), and an RTHS. The objective is to utilize the proposed RTHS predictive stability indicator (PSI) together with the predictive performance indicator (PPI) to conduct a successful RTHS where, (1) the performance of

the transfer system (i.e. a servo hydraulic actuator) is controlled (or compensated) relatively poorly, see Fig. 4.11, (2) the reference structure has a relatively large natural frequency ($\omega_n = 32.9\frac{rad}{sec}$) and it is lightly damped ($\zeta = 0.014$), see Fig. 4.4. In this experiment, that $\Omega = \tau\omega_n$ is relatively

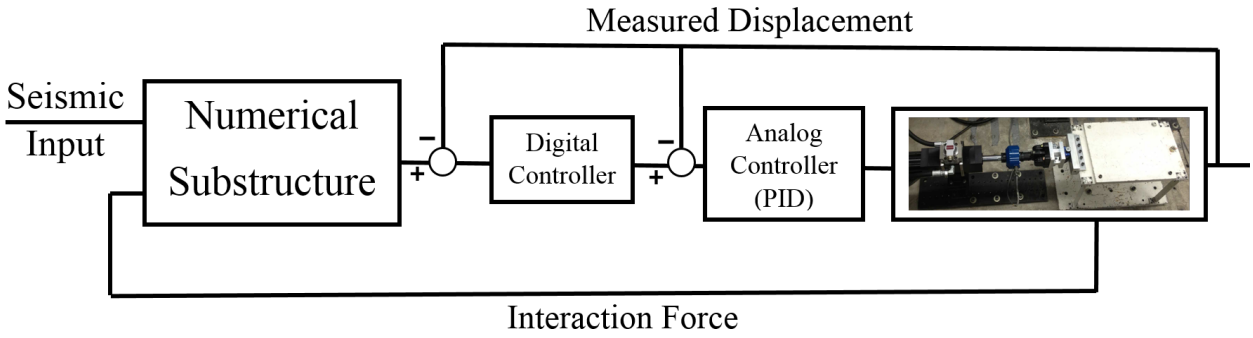

Figure 4.8: Real-time hybrid simulation.

large and ζ is relatively small make conducting a successful RTHS challenging. The sampling frequency, computational delay, communication delay, and approximated transfer system delay are 4096 Hz, 0.12 msec, 0.24 msec, and 14.4 msec, respectively. Having assigned ζ and Ω, the only influential parameter which can increase the PSI, reduce the PPI, and eventually enables a more successful RTHS is $|\gamma - \alpha|$.

First, a comparison is made between the shake table response of the reference structure and the response of its SDOF model while the exciting input is chosen to be the ChiChi earthquake history with the peak ground acceleration (PGA) of 0.061g, see Fig. 4.9. Validation of the reference model is necessary to obtain reliable values for $\{M, C, K\}_{REF}$ and eventually $\{\alpha, \beta, \gamma\}$.

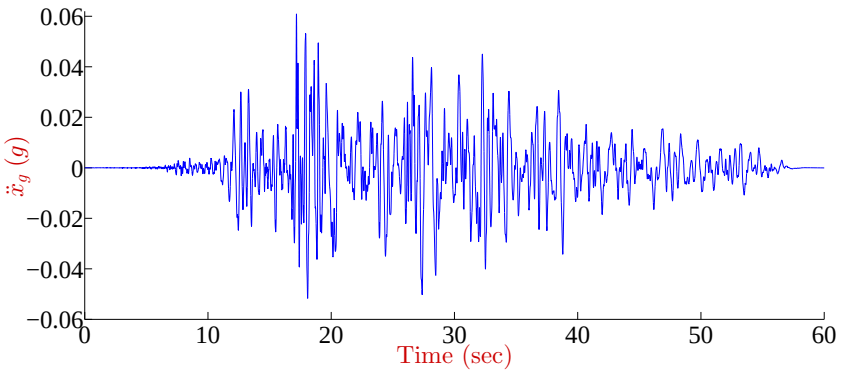

Figure 4.9: ChiChi earthquake ground acceleration with PGA = 0.061g.

Fig. 4.10 shows the comparison of the shake table response of the reference structure and the response of the reference model. To quantify the associated modeling error, the following error

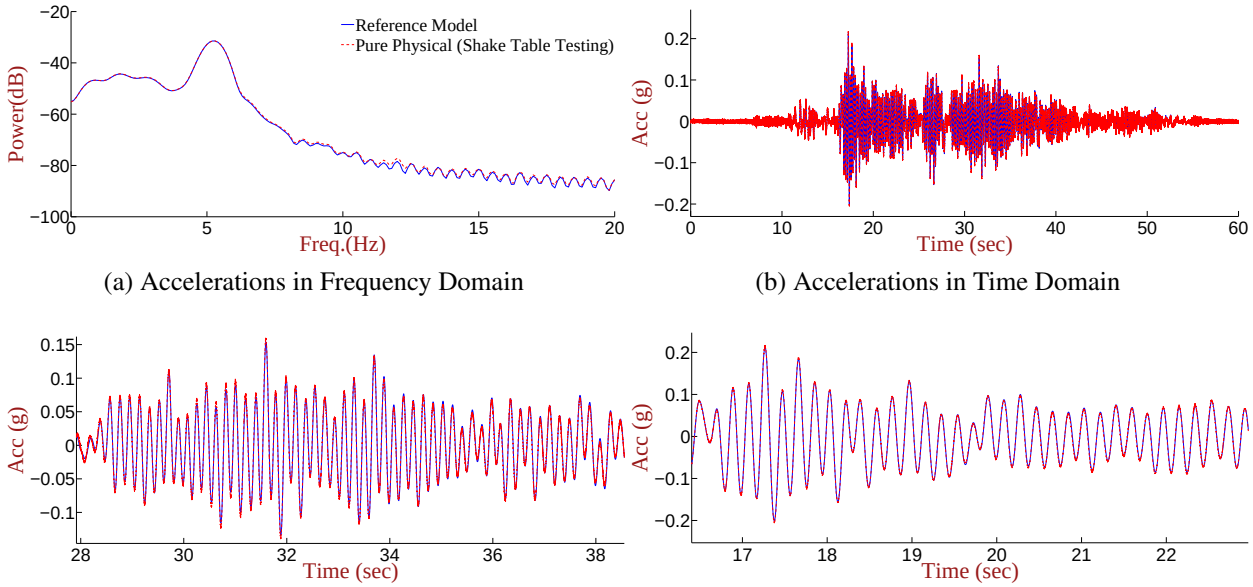

(a) Accelerations in Frequency Domain

(b) Accelerations in Time Domain

(c) Accelerations in Time Domain (zoomed-in)

(d) Accelerations in Time Domain (zoomed-in)

Figure 4.10: Comparison of the responses of the reference model with those of the pure physical (shake table) testing in the frequency and time domains.

indicator is utilized.

$$NRMSE\% = \frac{RMS[\ddot{x}_{SIM}(t) - \ddot{x}_{PHY}(t)]}{max[\ddot{x}_{PHY}(t)] - min[\ddot{x}_{PHY}(t)]} \times 100 \tag{4.3}$$

The corresponding normalized root-mean-square error (NRMSE) is 0.9%. The low NRMSE along with an excellent agreement in the frequency domain, see Fig. 4.10a, verify the fidelity of the reference model.

Table 4.3: Reference and substructures' characteristics

	Reference	Physical	Numerical	Partitioning Parameter
M(kg)	98.4	24.6	73.8	$\alpha = 0.75$
C$(N.s.m^{-1})$	88.7	15.8	72.9	$\beta = 0.82$
K$(N.m^{-1})$	10.67×10^4	2.67×10^4	8.00×10^4	$\gamma = 0.75$

Next, to conduct RTHS, we first evaluate the performance of the transfer system. In Fig. 4.11, the frequency responses of the hydraulic actuator identified using band-limited white noise input and a pure time delay system are shown. After identifying the reference structure and transfer system performance, we are ready to partition the reference structure and utilize the RTHS stability

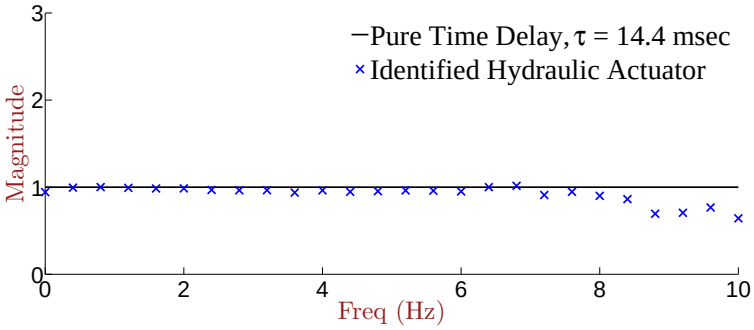

(a) Magnitude Plot

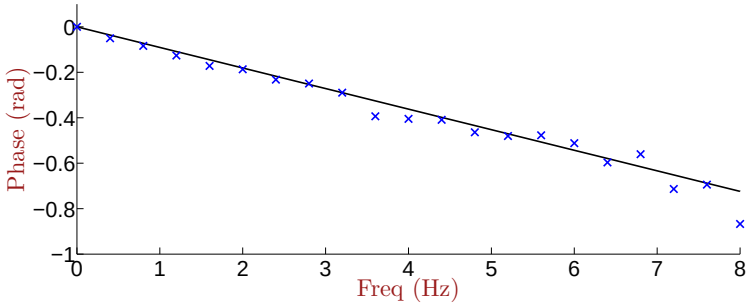

(b) Phase Plot

Figure 4.11: Frequency responses of the hydraulic actuator and a pure time delay system.

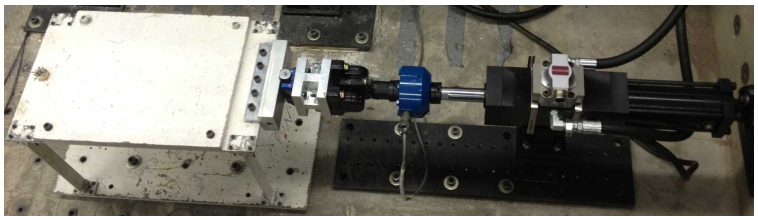

Figure 4.12: Physical substructure and transfer system used in this RTHS example.

switch criterion and the predictive stability and performance indicators. The structural characteristics of the reference structure, the physical substructure, and the numerical substructure are listed in Table 4.3. This RTHS configuration, $\{\zeta,\ \omega_n,\ \alpha,\ \beta,\ \gamma\}$ = $\{1.37\%,\ 32.9\ \frac{rad}{sec}$,0.75, 0.82, 0.75$\}$ minimizes the value of $|\gamma - \alpha|$ which enables a more successful RTHS.

In the RTHS setup shown in Fig. 4.8, $\{f_s,\ \tau_{COMP},\ \tau_{COMM},\ \tau_{TS}\}$ is set to be $\{$4096 Hz, 0.12 msec, 0.24 msec, 14.4 msec$\}$. Thus, the feedback time delay can be approximated as 14.8 msec. By knowing τ, ω_n, and the partitioning parameters, one can locate the corresponding RTHS case on the RTHS stability diagram. In Fig. 4.13, the case is indicated with a blue cross-mark and labeled as RTHS (Experimental Case). Using the PSI, one can predict that the partitioning choice in Table 4.3 and Ω = 0.49 leads to unconditional stability (PSI = ∞). As shown in Fig. 4.13,

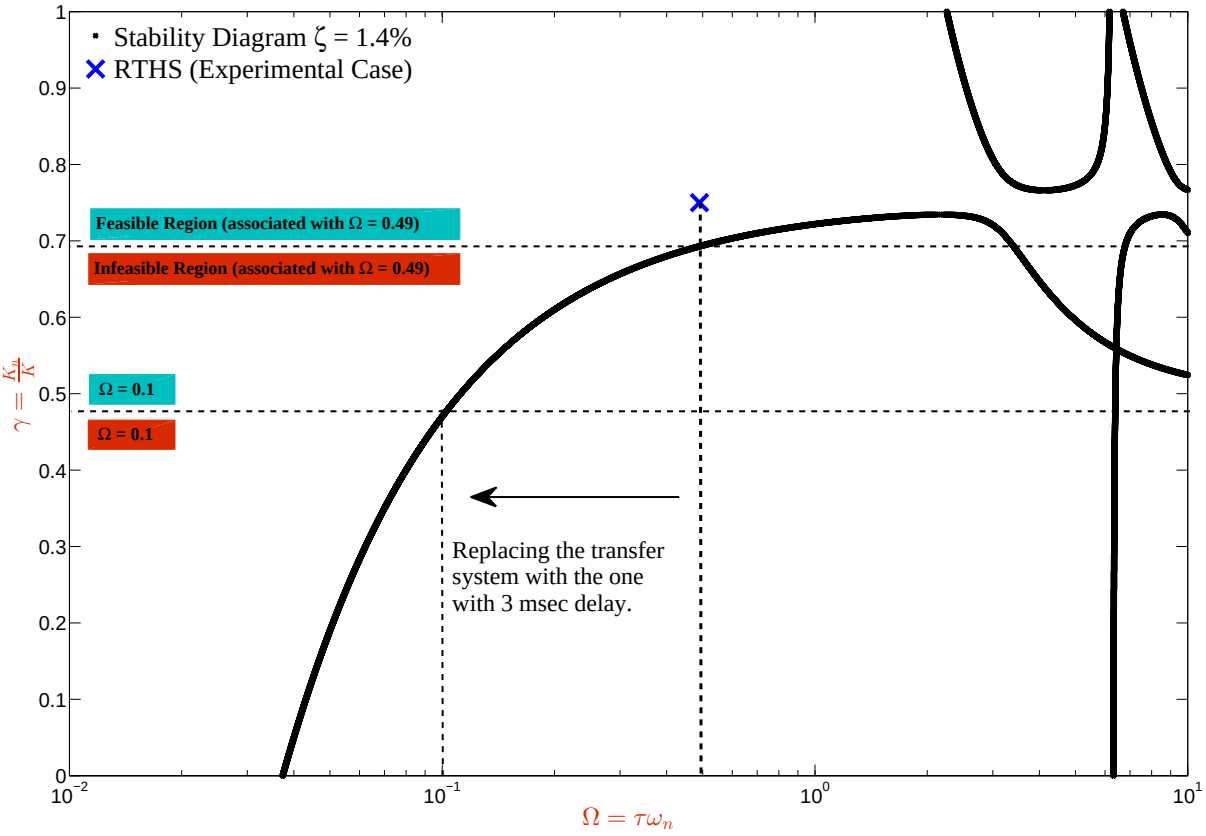

Figure 4.13: Location of the RTHS case study and simulation cases on the RTHS stability diagram.

$\Omega = \tau\omega_n = 0.49$ divides the diagram into two sections, feasible region ($0.69 < \gamma < 1$) and infeasible region ($0 < \gamma < 0.69$), and the RTHS case study in Table 4.3 lies within the feasible region ($\gamma = 0.75$).

In Fig. 4.14a, the RTHS case is indicated on the performance diagram. Fig. 4.14a also shows that, from performance perspectives, for these specific values of α, β, ζ, and Ω, $\gamma = \alpha = 0.75$ is the best choice since it minimizes the predictive sperformance indicator (PPI = 0.205). Furthermore, in Fig. 4.14b, γ is plotted versus $(\zeta - \zeta_{eff}) \times 10^3$ in which ζ_{eff} is obtained using Eq. (3.13) and the reference structure's damping (ζ) is 0.014. Fig. 4.14b confirms that for the specified values of α, β, ζ, and Ω, $\gamma = \alpha = 0.75$ is the best choice (i.e. $\zeta_{eff} \approx \zeta$). With this configuration, even though τ is relatively large, RTHS can be effectively conducted with accurate results.

Finally, an RTHS is conducted with the partitioning parameters listed in Table 4.3. The RTHS set-up is shown in Fig. 4.12 and the comparison of the RTHS results with the reference model results are shown in Fig. 4.15. To quantify the error developed in the RTHS results, the following

post-experiment indicator is used.

$$NRMSE\% = \frac{RMS[x_{SIM}(t) - x_{RTHS}(t)]}{max[x_{SIM}(t)] - min[x_{SIM}(t)]} \times 100 \tag{4.4}$$

Using Eq. (4.4) leads to an NRMSE of 0.8%. Having a low NRMSE value shows that conducting an RTHS with a low PPI value leads to a successful RTHS despite being restricted to a poor transfer system performance, the reference structure being lightly damped, and the reference structure having a relatively large natural frequency. Therefore, the proposed predictive indicators can be used as effective pre-experiment metrics in conducting SDOF RTHS.

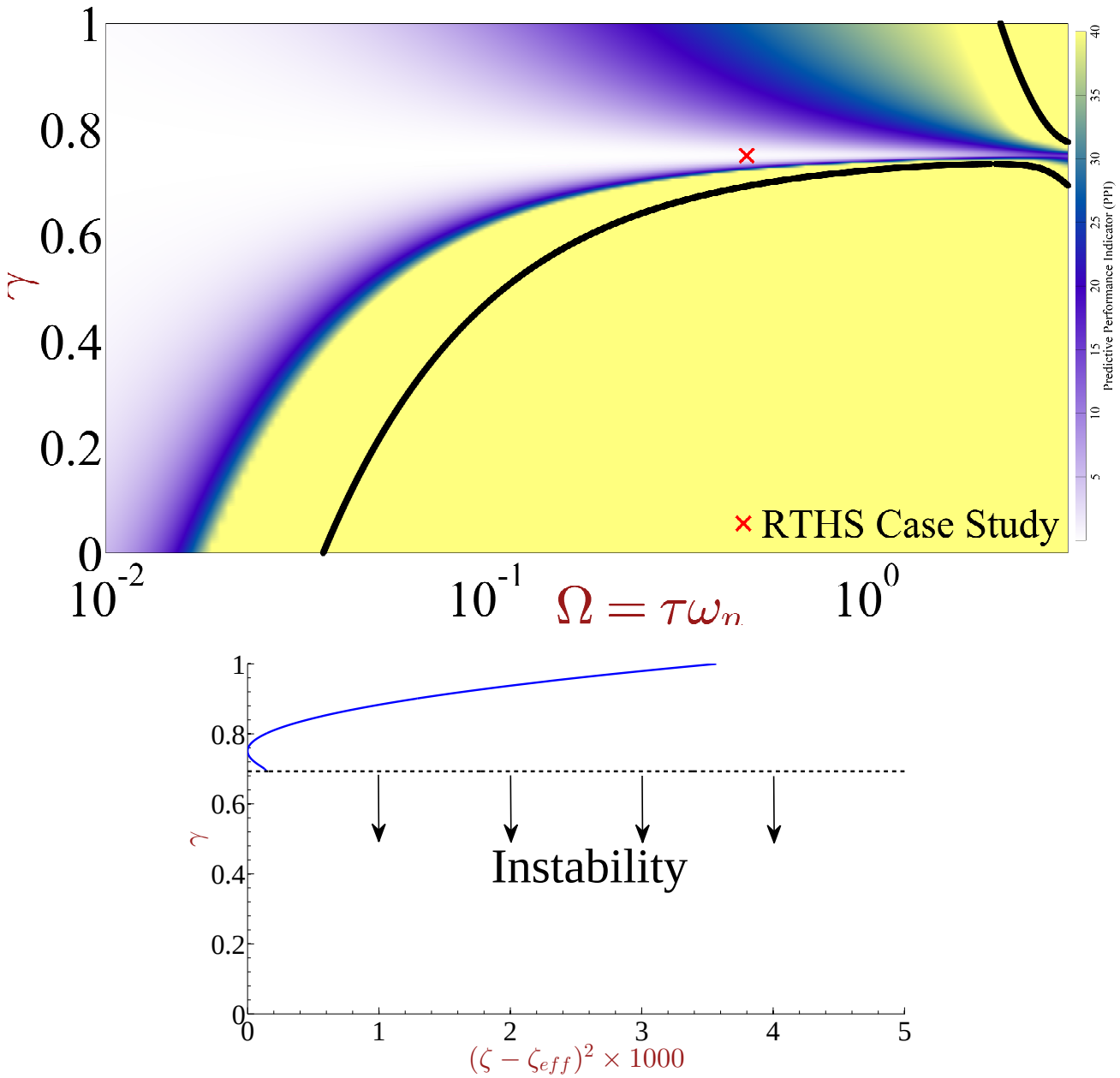

Figure 4.14: Selection of a Partitioning Parameter (γ) Using the RTHS Performance Diagram and the proposed Effective Damping.

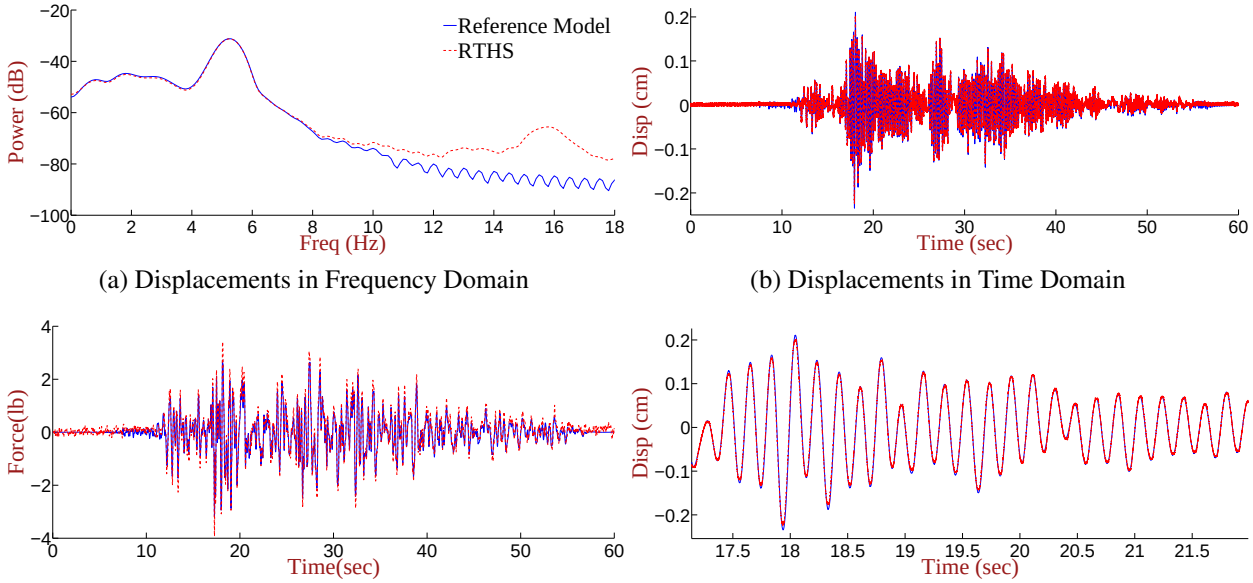

(a) Displacements in Frequency Domain

(b) Displacements in Time Domain

(c) Feedback Force in Time Domain

(d) Displacements in Time Domain (zoomed-in)

Figure 4.15: Comparison of the reference model and RTHS responses (relative displacements) of the single story structure in the time and frequency domains.

Chapter 5

Conclusion

In this study, new predictive (or pre-experiment) stability and performance indicators, the PSI and PPI, have been proposed to accommodate the impact of partitioning choices while considering the dynamics of transfer system, and the computational and communication delays. To fully leverage the capabilities of RTHS, guidelines are needed to address some key issues associated with its use. In this work, the major issues investigated are the minimum requirements of the transfer system control, the minimum required sampling frequency, the structural characteristics of the reference structure, the most effective changes to stabilize an unstable simulation due to the transfer system limitations, and nonlinearity in the physical substructure. Moreover, this study introduced the RTHS stability switch criterion which serves as an experimental design guideline associated with the minimum stability/control requirements to conduct a successful RTHS. With respect to the selection of partitioning parameters and the sources of systematic error, these metrics enable researchers to predict the stability margin and the expected accuracy of SDOF RTHS in the presence of reference responses. Moreover, in the absence of reference responses, the PPI can be used to effectively assess the accuracy of the results. Using the proposed predictive stability indicator along with the predictive performance indicator, we have been able to develop the normalized performance/stability diagrams appropriate for developing SDOF RTHS guidelines and acceptance criteria. In this study, the use of the proposed indicators is demonstrated in the three illustrative examples, vRTHS with pure time delay, vRTHS with time delay and transfer system dynamics, and an experimental SDOF RTHS. The results show that the PSI and PPI can be effectively used to predict the susceptibility of a SDOF RTHS configuration to transfer system dynamics and computational/communication delays.

Bibliography

Ahmadizadeh, M. (2007). *Real-time Seismic Hybrid Simulation Procedures for Reliable Structural Performance Testing*. Ph. D. thesis, University of New York at Buffalo.

Astrom, K. J. and B. Wittenmark (1990). *Computer-controlled Systems: Theory and Design*. Prentice Hall, Englewood Cliffs, New Jersey.

Beretta, E. and Y. Kuang (2002, January). Geometric Stability Switch Criteria in Delay Differential Systems with Delay Dependent Parameters. *SIAM Journal on Mathematical Analysis 33*(5), 1144–1165.

Carrion, J. E. and B. F. Spencer (2007). Model-based Strategies for Real-time Hybrid Testing. Technical Report December, Newmark Structural Engineering Laboratory. University of Illinois at Urbana-Champaign.

Castaneda, N., X. Gao, and S. J. Dyke (2012). A Real-time Hybrid Testing Platform for the Evaluation of Seismic Mitigation in Building Structures. In *Proc. of the 2012 Structures Congress Conference*.

Chae, Y. (2011). *Seismic Hazard Mitigation of Building Structures Using Magneto-Rheological Dampers*. Ph. D. thesis, Lehigh University.

Chen, C. and J. M. Ricles (2009a, November). Analysis of Actuator Delay Compensation Methods for Real-time Testing. *Engineering Structures 31*(11), 2643–2655.

Chen, C. and J. M. Ricles (2009b, August). Improving the Inverse Compensation Method for Real-time Hybrid Simulation through a Dual Compensation Scheme. *Earthquake Engineering & Structural Dynamics 38*(10), 1237–1255.

Chen, C., J. M. Ricles, T. L. Karavasilis, Y. Chae, and R. Sause (2012, February). Evaluation of a Real-time Hybrid Simulation System for Performance Evaluation of Structures with Rate Dependent Devices Subjected to Seismic Loading. *Engineering Structures 35*, 71–82.

Chen, C., J. Valdovinos, and H. Santiallno (2013, April). Reliability Assessment of Real-Time Hybrid Simulation Results for Seismic Hazard Mitigation. In *Proc. of Structures Congress 2013*, Reston, VA, pp. 2346–2357. American Society of Civil Engineers.

Christenson, R., Y. Z. Lin, A. Emmons, and B. Bass (2008, April). Large-Scale Experimental Verification of Semiactive Control through Real-Time Hybrid Simulation. *Journal of Structural Engineering 134*(4), 522–534.

Darby, A. P., A. Blakeborough, and M. S. Williams (2001, March). Improved Control Algorithm for Real-time Substructure Testing. *Earthquake Engineering & Structural Dynamics 30*(3), 431–448.

Darby, A. P., M. S. Williams, and A. Blakeborough (2002, December). Stability and Delay Compensation for Real-Time Substructure Testing. *Journal of Engineering Mechanics 128*(12), 1276–1284.

Dihoru, L. and A. Bonzi (2010). Performance Requirements of Actuation Systems for Shaking Table and Pseudo-Dynamic Testing. *SERIES: Seismic Engineering Research Infrastructures for European Synergies.*.

Dyke, S. J., B. F. Spencer, M. K. Sain, and J. D. Carlson (1996, October). Modeling and control of magnetorheological dampers for seismic response reduction. *Smart Materials and Structures 5*(5), 565–575.

Dyke, S. J., B. F. Spencer, M. K. Sain, and J. D. Carlson (1998, October). An experimental study of MR dampers for seismic protection. *Smart Materials and Structures 7*(5), 693–703.

Dyke, S. J., B. F. Spencer Jr., P. Quast, and M. K. Sain (1995, February). Role of Control-Structure Interaction in Protective System Design. *Journal of Engineering Mechanics 121*(2), 322–338.

Dyke, S. J., B. Stojadinovic, P. Arduino, M. Garlock, N. Luco, J. A. Ramirez, and S. Yim (2010). 2020 Vision for Earthquake Engineering Research: Report on an OpenSpace Technology Workshop on the Future of Earthquake Engineering. Technical Report 5, Network for Earthquake Engineering Simulation (NEES).

Friedman, A. J., J. Zhang, B. Phillips, Z. Jiang, A. Agrawal, S. J. Dyke, J. Ricles, B. Spencer, R. Sause, and R. Christenson (2010). Accommodating MR Damper Dynamics for Control of Large Scale Structural Systems. Technical report.

Gao, X. (2012). *Development of a Robust Framework for Real-Time Hybrid Simulation: from Dynamical System, Motion Control to Experimental Error Verification*. Ph. D. thesis.

Horiuchi, T., M. Inoue, T. Konno, and W. Yamagishi (1999). Development of a Real-time Hybrid Experimental System Using a Shaking Table (Proposal of Experimental Concept and Feasibility Study with Rigid Secondary System). *JSME International 42*(2), 255–264.

Horiuchi, T., M. Nakagawa, M. Sugano, and T. Konno (1996). Development of a Real-time Hybrid Experimental System with Actuator Delay Compensation. In *Proc. of 11th World Conf. Earthquake Engineering*.

Jiang, Z. and R. Christenson (2011, June). A Comparison of 200 kN Magneto-rheological Damper Models for Use in Real-time Hybrid Simulation Pre-testing. *Smart Materials and Structures 20*(6), 065011.

Karnopp, D., M. J. Crosby, and R. A. Harwood (1974). Vibration Control Using Semi-Active Force Generators. *Journal of Engineering for Industry 96*(2), 619.

Li, J., D. Ferry, K. Kieselbach, A. Saifullah, K. Agrawal, C. D. Gill, and C. Lu (2013). Practical Real-time Scheduling for Parallel Tasks from Theory to Platform.

MacDonald, N. (1989). *Biological Delay Systems: Linear Stability Theory*. Cambridge: Cambridge University Press.

Maghareh, A., S. J. Dyke, G. Ou, and Y. Qian (2013, January). Investigation of Uncertainties Associated with Actuation Modeling Error and Sensor Noise on Real-time Hybrid Simulation Performance. In *Proc. of 2013 International Conference on Computing, Networking and Communications (ICNC)*, pp. 210–214. IEEE.

Maghareh, A., S. J. Dyke, A. Prakash, G. Bunting, and P. Lindsay (2012). Evaluating Modeling Choices in the Implementation of Real-time Hybrid Simulation. In *Proc. of EMI/PMC 2012 Joint Conference of the Engineering Mechanics Institute and the 11th ASCE Joint Specialty Conference on Probabilistic Mechanics and Structural Reliability*, Notre Dame, IN.

Maghareh, A., S. J. Dyke, A. Prakash, and G. B. Bunting (2013). Establishing a Predictive Performance Indicator for Real-time Hybrid Simulation. *Earthquake Engineering & Structural Dynamics* (submitted).

Maghareh, A., S. J. Dyke, A. Prakash, and J. F. Rhoads (2013). Establishing a Stability Switch Criterion for Effective RTHS Implementation. *Journal of Smart Materials and Structures* (in press).

Mahin, S. A., P. B. Shing, C. R. Thewalt, and R. D. Hanson (1989, August). Pseudodynamic Test MethodCurrent Status and Future Directions. *Journal of Structural Engineering 115*(8), 2113–2128.

Mosqueda, G., B. Stojadinovic, and S. Mahin (2005). Implementation and Accuracy of Continuous Hybrid Simulation with Geographically Distributed Substructures. Technical Report November.

Mosqueda, G., B. Stojadinovic, and S. A. Mahin (2007a). Real-Time Error Monitoring for Hybrid Simulation. Part I: Methodology and Experimental Verification. *Journal of Structural Engineering 133*(8), 1100–1108.

Mosqueda, G., B. Stojadinovic, and S. A. Mahin (2007b). Real-Time Error Monitoring for Hybrid Simulation. Part II: Structural Response Modification due to Errors. *Journal of Structural Engineering 133*(8), 1109–1117.

Nakashima, M., H. Kato, and E. Takaoka (1992). Development of real-time pseudo dynamic testing. *Earthquake Engineering & Structural Dynamics 21*(1), 79–92.

Nakashima, M. and N. Masaoka (1999, April). Real-time on-line Test for MDOF Systems. *Earthquake Engineering & Structural Dynamics 28*(4), 393–420.

Ou, G., S. J. Dyke, B. Wu, A. I. Ozdagli, and B. Li (2013). Robusted Integrated Actuator Control Strategy for Real Time Hybrid Simulation. In *Proc. of SERIES Concluding Workshop - Joint with US-NEES "Earthquake Engineering Research Infrastructures"*, Ispra.

Phillips, B. M. and B. F. Spencer (2013, February). Model-Based Multiactuator Control for Real-Time Hybrid Simulation. *Journal of Engineering Mechanics 139*(2), 219–228.

Schellenberg, A. and S. Mahin (2006). Integration of Hybrid Simulation within the General-purpose Computational Framework OpenSees. In *Proc. of 100th Anniversary Earthquake Conference*.

Shao, X., A. M. Reinhorn, and M. V. Sivaselvan (2011, July). Real-Time Hybrid Simulation Using Shake Tables and Dynamic Actuators. *Journal of Structural Engineering 137*(7), 748–760.

Shing, P. B. and S. A. Mahin (1984). Pseudodynamic Test Method for Seismic Performance Evaluation: Theory and Implementation. Technical report, Earthquake Engineering Research Center, University of California, Berkeley.

Shing, P. B., M. Nakashima, and O. S. Bursi (1996). Application of Psuedodynamic Test Method to Structural Research. *Earthquake Spectra 12(1)*, 29–56.

Shing, P. B., Z. Wei, R. Y. Jung, and E. Stauffer (2004). NEES Fast Hybrid Test System at the University of Colorado. In *Proc. of 13th World Conference on Earthquake Engineering*, Number 3497.

Takanashi, K. and M. Nakashima (1987, July). Japanese Activities on OnLine Testing. *Journal of Engineering Mechanics 113*(7), 1014–1032.

Wagg, D. J. and D. P. Stoten (2001, June). Substructuring of Dynamical Systems via the Adaptive Minimal Control Synthesis Algorithm. *Earthquake Engineering & Structural Dynamics 30*(6), 865–877.

Wallace, M. I., J. Sieber, S. A. Neild, D. J. Wagg, and B. Krauskopf (2005, December). Stability Analysis of Real-time Dynamic Substructuring Using Delay Differential Equation Models. *Earthquake Engineering & Structural Dynamics 34*(15), 1817–1832.

Zhao, J., C. French, C. Shield, and T. Posbergh (2003, September). Considerations for the Development of Real-time Dynamic Testing Using Servo-hydraulic Actuation. *Earthquake Engineering & Structural Dynamics 32*(11), 1773–1794.